IN-SITU GROWTH AND CHARACTERIZATION OF EPITAXIAL NI FILMS ON MGO SUBSTRATES

YU JINHUA

(B.Eng., Shanghai Jiao Tong University, P.R.China)

A THESIS SUBMITTED

FOR THE DEGREE OF MASTER OF SCIENCE

DEPARTMENT OF MATERIALS SCIENCE

NATIONAL UNIVERSITY OF SINGAPORE

2003

ACKNOWLEDGEMENTS

It is my pleasure to thank many people who made this thesis possible.

Firstly, I would like to express my sincere appreciation to my supervisor, Dr. Mark Yeadon, for his continuous guidance, enthusiasm, inspiration and his great efforts to explain things clearly. Throughout my thesis-writing period, he provided encouragement, sound advice, good teaching, and lots of good ideas. I would have been lost without him.

Also, I would like to thank Dr. Chris Boothroyd (IMRE) who has taught me a lot on the crystal structure analysis during my postgraduate study and the thesis writing period as well. It is impossible for me to finish the analysis work without his help! I also thank Prof. R. A. Lukaszew (University of Toledo, Ohio) who has performed MOKE analysis for us.

I am indebted to many of my colleagues for providing a stimulating and fun environment in which to learn and grow. I'm especially grateful to Suey Li, Shue Yin, Lin Ming, Ramesh and Chi Wen.

I wish to thank my best friend Gong Zheng, for helping me get through difficult times, and for all the emotional support, and for the comradery.

Lastly, but not least, I wish to thank my parents and my fiancé. They support me, teach me and love me. To them I dedicate this thesis.

TABLE OF CONTENTS

Acknowledgements I

Table of Contents II

Summary V

List of Tables VI

List of Figures VII

List of Publications XI

Chapter 1 Introduction

1.1 Thin Film Growth 1

1.1.1 Homoepitaxy and Heteroepitaxy 1

1.1.2 Nucleation and Growth Modes 5

1.1.3 Evolution of Growth 8

1.2 Thin Film Deposition Techniques 10

1.2.1 Evaporation Method 10

1.2.2 Sputtering 11

1.2.3 MBE 12

1.3 Ni and MgO 13

1.4 Magnetic Property of Thin Films---(MOKE) 15

1.4.1 Introduction 15

1.5 *In-situ* Transmission Electron Microscopy 18

References 20

Chapter 2 Literature Review

2.1 Previous Studies of Ni on MgO 22

2.1.1 Lattice Mismatch 22

2.1.2 Film Thickness 24

2.1.3 Growth Temperature 25

2.1.4 Annealing 26

2.2 Magnetic Properties 27

References 29

Chapter 3 Experiment

3.1 Principles of Transmission Electron Microscopy 30

3.1.1 Optical System 31

3.1.2 Selected-area Diffraction 32

3.1.3 Bright field and Dark field imaging 35

3.2 Introduction to the MERLION system 36

3.2.1 Sample Loading System 38

3.2.2 Experiment System 39

3.3 Sample Preparation 40

3.3.1 MgO (100) Preparation 40

3.3.2 Si Preparation 40

3.3.3 Sample Mounting 41

3.3.4 Heating of MgO substrate and Calibration of Temperature 41

3.4 MOKE Experimental Arrangements 42

References 44

Chapter 4 Results & Discussion (1): Crystal Structure

4.1 Initial Nucleation and growth of Ni on MgO (100) 45

4.1.1 *hcp* Ni Phase 47

4.1.2 Transformation from *hcp* Ni to *fcc* Ni 51

4.2 Phase Composition as a function of Temperature 55

4.3 High Temperature annealing of Ni deposits 60

References 65

Chapter 5 Results & Discussion (2): Surface diffusion, Island coalescence and Magnetic properties

5.1 Activation Energy for surface diffusion 66

5.2 Island Coalescence 68

5.3 Magnetic Properties (MOKE) 72

References 77

Chapter 6 Conclusion 78

Summary

Heteroepitaxial growth is a classical yet constantly evolving subject with great opportunities for practical applications. From quantum wells to semiconductor nano-structures, this special form of crystal growth has revolutionized opto-electronic materials technology and is beginning to impact the new frontier of spintronics. Epitaxial Ni/insulator interfaces are of growing interest, and their application concerns many different industrial sectors, such as thin film elaboration, electronic and opto-electronic devices and glass industry. This research mainly focused on the crystal structures and magnetic properties of Ni/MgO heteroepitaxial films.

The most interesting result in these experiments was the observation of a novel hexagonal close-packed (*hcp*) phase of Ni structure, which does not exist in Nature. The *hcp* phase was stabilized due to a pseudomorphic layer of Ni, where Ni-O bonds were formed as the first monolayer of Ni was deposited. A transformation from *hcp* Ni to *fcc* Ni during growth then occurred at a nominal substrate coverage of between 3.6 to 4.8nm. During higher temperature annealing after growing at 100°C, a structure transformation from *hcp* Ni to (110) *fcc* Ni can also be observed at 720°C.

A four-fold symmetry magnetic anisotropy was detected for the as-grown sample without annealing by the MOKE system; while, for the annealed sample, uniaxial anisotropy was observed.

List of Tables

Table 5.1 Saturation island nucleation densities at different growth temperatures.

List of Figures:

Figure 1.1 Schematic illustration of (a) lattice-matched, (b) strained, and (c) relaxed heteroepitaxial structures. Homoepitaxy is structurally very similar to lattice-matched heteroepitaxy.

Figure 1.2 Schematic representation of the three growth modes, as a function of the coverage θ in ML: (a) island, or Volmer-Weber growth; (b) layer-plus-island, or Stranski-Krastanov growth; (c) layer-by-layer, or Frank-van der Merwe growth.

Figure 1.3 (a) Growth of A on B, where $\gamma_A < \gamma_B$; misfit dislocations are introduced, or islands from after a few layers have been deposited; (b) Growth of B directly onto A as islands. The interfacial energy γ^* represents the excess energy over bulk A and B integrated through the interface region; (c) Surface processes and characteristic energies in nucleation and film growth.

Figure 1.4 Schematic representation of processes leading to three-dimensional nucleation and film growth.

Figure 1.5 Schematic diagram showing free energy versus the radius r of a spherical nuclei.

Figure 1.6 (a) Solid state structure of MgO; (b) Simulated <100> orientation diffraction pattern of MgO (001); (c) Solid state structure of Ni; (d) simulated <100> orientation diffraction pattern of Ni (001), of the same camera length with (b).

Figure 1.7 Thermal expansion coefficient of MgO.

Figure 1.8 The orientation of the magnetization with respect to the scattering plane for each of the three principle geometries for the Kerr effect. The polar and longitudinal geometries describe the magnetization M in the scattering plane, normal and parallel to the sample surface respectively. The transverse (equatorial) geometry describes the case where the magnetization is perpendicular to the scattering plane but in the plane of the sample surface.

Figure 2.1 Epitaxial orientations of alkali halides, chalcogenide compounds and metals on (001)MgO with reference to the lattice parameter ratio $\rho = a_d/a_s$ (d:deposit and s:substrate). The sizes of the orientation symbols roughly represent relative preferences.

Figure 3.1 TEM illumination system.

Figure 3.2 Schematic of diffraction pattern and SAD pattern. (a) projecting the diffraction pattern on the viewing screen; (b) showing SAD pattern formation: the insertion of an aperture in the image plane results in the creation of a virtual aperture in the plane of the specimen, only electrons falling inside the dimensions of the virtual aperture at the specimen will be allowed through into the imaging system, all other electrons will hit the SAD diaphragm.

Figure 3.3 The relationship between the spacing R of diffraction maxima and camera length,L.

Figure 3.4 Ray diagrams showing how the objective lens/aperture are used in combination to produce (a) a BF image formed from the direct beam; (b) a CDF image where the incident beam is tilted so that the scattered beam remains on axis. The area selected by the objective aperture, as seen on the viewing screen, is shown below each ray diagram.

Figure 3.5 MERLION system.

Figure 3.6 Schematic view of MERLION system.

Figure 3.7 Schematic view of MERLION sample loading system.

Figure 3.8 Evaporator fitting a rod.

Figure 3.9 Schematic of the procedure of sample preparation.

Figure 3.10 MgO current-temperature plot (the temperatures are measured by pyrometer), x-axis indicates the heating current, unit: mA; y axis indicates the substrate temperature, unit: ^{o}C.

Figure 3.11 A schematic of a dc arrangement for observing the Kerr effect. The incident (laser) beam is polarized and incident at an angle β (typically 20˚) with respect to the sample normal ***n***. The sample can be rotated about the normal so that the angle between the applied field ***H*** and a specific crystal axis **G** can be vaired. The polarization is analysed by a polariser with transmission direction aligned at an angle α with respect to the scattering plane normal. The detector is not shown.

Figure 4.1 Computer simulations for the SAED pattern (a) simulation of the [001] zone axis SAED pattern of MgO; (b) simulation of the [001] zone axis SAED pattern of Ni; (c) superposition of (a) and (b).

Figure 4.2 Computer simulations for the SAED pattern: (a) simulation of the [001] zone axis SAED pattern of MgO; (b) simulation of the $[11\bar{2}0]$ zone axis SAED pattern of *hcp*-Ni; (c) simulation of the $[11\bar{2}0]$ zone axis SAED pattern of an orthogonal growth variant, e.g. a 90° rotation counterpart to (b); (d) superposition of (a)(b)(c).

Figure 4.3 Diagram showing the arrangement of the first two monolayers of Ni grown on (001) MgO.

Figure 4.4 SADP indicating a Ni (110) epitaxial relationship, with the bold white circle indicating the orientation of Ni $[\bar{1}1\bar{1}]$//MgO [100], the regular white circle indicating a mirror relationship to the bold white circle along the MgO [010] direction.

Figure 4.5 A schematic illustration of an *hcp→fcc* martensitic phase transformation through the staking faults mechanism.

Figure 4.6 A sequence of selected area diffraction patterns recorded at a film thickness of 5nm at temperatures of (a)→(e): 25ºC, 50ºC, 100ºC, 300ºC and 550ºC, respectively.

Figure 4.7 Phase diagram as a function of growth temperature and thickness, for Ni on MgO (100).

Figure 4.8 SADPs as a function of temperature following deposition of a Ni layer of nominal thickness 0.8nm at 100ºC. (a) sadp immediately after completion of Ni growth; (b) sadp at the annealing temperature of 650ºC; (c) sadp at the annealing temperature of 720ºC.

Figure 4.9 Bright field image and diffraction pattern comparison before and after anneal: (a) bf image before anneal; (b) bf image after anneal; (c) diffraction pattern before anneal; (d) diffraction pattern after anneal.

Figure 5.1 Arrhenius plot of Log (saturation nucleation density) as a function of 1000/T_g, where T_g is the growth temperature.

Figure 5.2 Bright field images recorded during the early stages of film growth at the point of maximum nuclei density (the saturation nucleation density) for substrate temperatures of (a) 50ºC and (b) 100ºC.

Figure 5.3 Images and diffraction patterns (inset), corresponding to the transition from *hcp* to *fcc* Ni during growth at 100ºC at different nominal thickness. (a) 0.21nm; (b) 0.3nm; (c) 0.45nm; (d) 0.75nm; (e) corresponding SAD pattern of image (a); (f) corresponding SAD pattern of image (d).

Figure 5.4 The Morié fringe shows the different orientation on one single island, temperature: 100ºC, nominal thickness: 37.4nm.

Figure 5.5 Bright field images of Ni films deposited at (a) and (b): 380ºC, (c) and (d): 550ºC, indicating the different coalescence phenomena under different growth temperatures.

Figure 5.6 Bright field images and sadps of the MOKE sample: (a) bf before annealing; (b) bf after 5h's annealing; (c) sadp before annealing; (d) sadp after 5h's annealing.

Figure 5.7 MOKE data obtained from Ni thin film of 100ºC growth temperature: (a) immediately after growth; (b) after annealed at a temperature of 300ºC *in-situ* for 5 hours.

List of Publications

1. **J. Yu**, W. Tian, H. Sun, X. Q. Pan, C. B. Boothroyd, A. Lukaszew, R. Clarke and M. Yeadon, *"Structural evolution of Ni thin films on MgO: Surface Energy Vs Strain Relaxation"* to be submitted.

2. W. Tian, H. Sun, **J. Yu**, M. Yeadon, C. B. Boothroyd, A. Lukaszew, R. Clarke and X. Q. Pan, *"Epitaxial Stabilization and Structural Evolution of Hexagonal Close-Packed Ni on Single Crystal MgO"* submitted to Phys. Rev. Lett.

3. H. P. Sun, W. Tian, Y. B. Chen, **J. Yu**, M. Yeadon, C. B. Boothroyd, R. Clarke, and X. Q. Pan, *"Epitaxial Growth and structural stability of Ni nanostructures on (001) MgO"* to be submitted.

CHAPTER 1 Introduction

1.1 Thin film growth

Epitaxial growth is a subject with considerable practical application, particularly in relation to the fabrication of semiconductor devices. For many years the phenomenon of epitaxy has been of substantial scientific and technological importance. The term epitaxy is derived from the Greek words επi (epi-placed or resting upon) and ταξιζ (taxis-arrangement), and refers to single-crystal film growth over a crystalline substrate. A variety of growth techniques have been employed such as vacuum evaporation (e.g. molecular beam epitaxy), sputtering, and electrodeposition. Particular interest has centered on epitaxial films exhibiting layer growth that results in the formation of relatively smooth films, which are particularly important, for example, in the fabrication of heterojunctions.

1.1.1 Homoepitaxy and Heteroepitaxy

Two types of epitaxy can be distinguished and each has important scientific and technological implications. *Homoepitaxy* refers to the case where the film and substrate are of the same material, such as the growth of Si on a Si wafer, or GaAs over a GaAs wafer. The epilayer generally has a lower density of defects and is of purer composition than the substrate, and can be doped independently. A dramatic improvement in the yield of early bipolar junction transistors (BJTs) was the result of

incorporating the epi-Si deposition step, where a layer of Si was grown homoepitaxially over the Si wafer, and the BJTs fabricated within this fresh layer.

The second type of epitaxy is known as *heteroepitaxy*[1] and refers to films and substrates composed of different materials. Heteroepitaxy is the more common phenomenon. Optoelectronic devices such as light-emitting diodes and lasers are based on compound semiconductor heteroepitaxial film structures.

The differences between the two basic types of epitaxy are schematically illustrated in Figure 1.1. When the materials epilayer and substrate crystals are of the same material and crystallographic orientation, the lattice parameters will naturally be perfectly matched, and no interfacial bond straining will be present. This situation is illustrated in Figure 1.1(a).

In the case of heteroepitaxial growth, the lattice parameters may not be perfectly matched, and, depending on the extent of the mismatch, we can envision three distinct epitaxial regimes. If the lattices are in fact perfectly matched, then the heterojunction interfacial structure may correspond to that of homoepitaxy (Figure 1.1(a)); in this case, the interface will be coherent and strain free. If there is a small degree of mismatch, then the interfacial structure may be coherent between the two structures, the lattice structure at the interfaces being strained to maintain coherency without the introduction of defects such as dislocations (Figure 1.1 (b)). Small lattice mismatch in heteroepitaxial systems may sometimes be achieved through careful control of the composition of the materials involved.

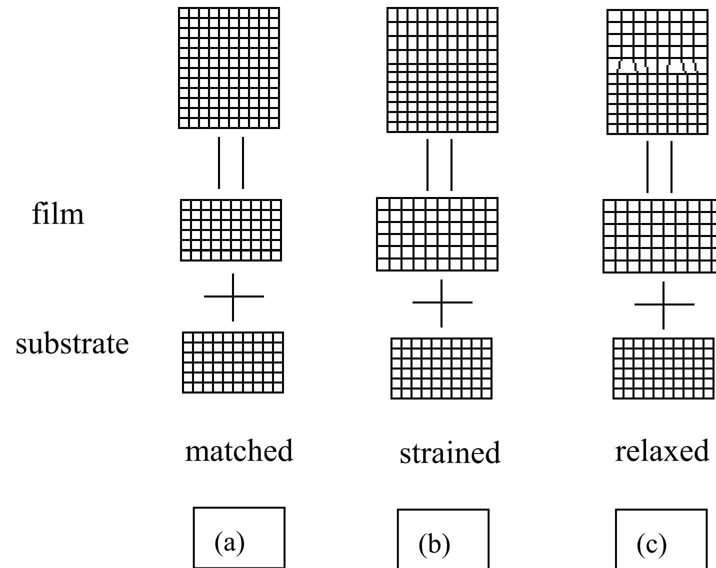

Figure 1.1 Schematic illustration of (a) lattice-matched, (b) strained, and (c) relaxed heteroepitaxial structures. Homoepitaxy is structurally very similar to lattice-matched heteroepitaxy.

When the film and substrate lattice parameters differ substantially, we may encounter the cases illustrated in Figure 1.1 (c). Here, the interface has become dislocated due to the presence of substantial lattice strain at the interface. Although energy is required in order to introduce the dislocation into the crystal lattice, the dislocation may still be introduced provided the strain energy relieved by this process exceeds the strain energy associated with the dislocation itself. Matthews[2,3] proposed that this process would occur at a critical film thickness d_c, which can be calculated by minimizing the sum of the elastic strain energy E_ε (per unit area) and dislocation energy E_d (per unit area) with respect to the film strain ε_f. Assuming that the film and substrate shear moduli, μ, are the same, we have approximate expressions for E_ε and E_d:

$$E_{\varepsilon}=\frac{2\mu(1+\nu)\varepsilon_f^2 d}{1-\nu} \tag{1}$$

$$E_d=\frac{\mu b(f-\varepsilon_f)\ln(\frac{R_0}{b}+1)}{2\pi(1-\nu)} \tag{2}$$

Where d is the film thickness, υ is Poisson's ratio, b is the dislocation Burgers vector, and R_0 is a radius about the dislocation where the strain field terminates. Taking the derivative of $E_{\varepsilon}+E_d$ with respect to ε_f and setting it equal to zero gives for the critical strain a value

$$\varepsilon_f^{\ 2}=\frac{b\ln(\frac{R_0}{b}+1)}{8\pi(1+\nu)d} \tag{3}$$

The largest possible value for ε_f^* is f. If the value of ε_f^* predicted is larger than f, the film will strain to match the substrate exactly. If $\varepsilon_f^* < f$, a portion of the misfit equal to $f-\varepsilon_f^*$ will be accommodated by misfit dislocations. By assuming that $\varepsilon_f^* \approx f$ at $d=d_c$ and that $R_0 \approx d_c$, the critical film thickness prior to misfit dislocation formation is expressed by:

$$d_c=\frac{b\ln(\frac{d_c}{b}+1)}{8\pi(1+\nu)f} \tag{4}$$

When the lattice misfit becomes larger, the spacing between misfit dislocations decreases to the order of only a few lattice spacings. In such a scenario, natural lattice misfit theory breaks down. There are no longer large areas of good fit separated by narrow regions of poor fit. Rather, poor fit occurs everywhere.

1.1.2 Nucleation and growth modes[4,5,6,7,8,9,10,11]

It is generally accepted that there are three possible modes of crystal growth on surfaces, which are illustrated schematically in Figure 1.2, following Venables et al[7] (1984). In the **Volmer-Weber** (or island) growth mode (Figure 1.2 (a)), small clusters of deposit nucleate directly on the substrate surface, which grow to form 3D islands of the condensed phase on the substrate surface. This process typically occurs when the atoms (or molecules) of the deposit are more strongly bound to each other than to the substrate. This mode is displayed by many systems of metals growing on insulators, including many metals on oxides, alkali halides, graphite and other layered compounds such as mica.

The **Frank-van der Merwe** (or 2D layer-by-layer) growth mode (Figure 1.2 (c)) is rather different. Because the atoms are more strongly bound to the substrate than to each other, the first atoms to condense form a complete monolayer on the surface, which becomes covered with a somewhat less tightly bound second layer. This growth mode is observed in the case of adsorbed gases, such as several rare gases on graphite and on several metals, in some metal-metal systems, and in the growth of some semiconductors systems.

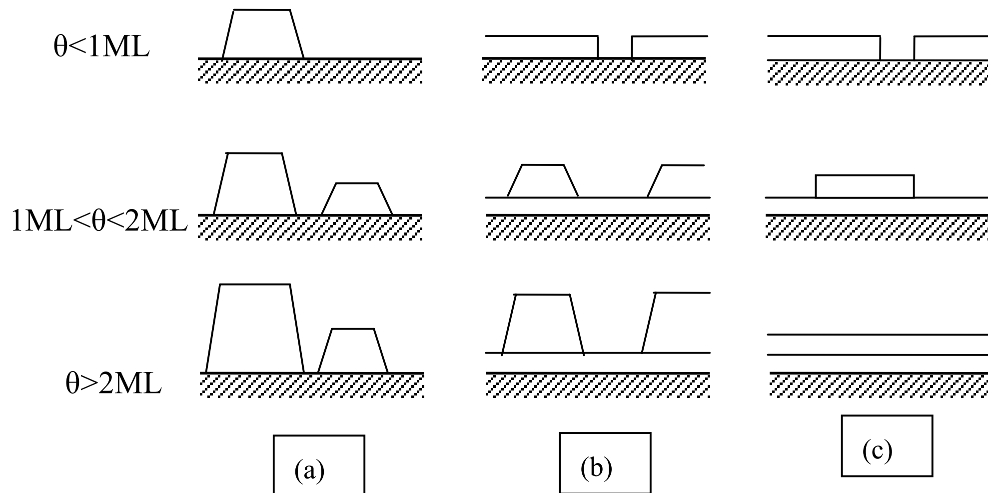

Figure 1.2 Schematic representation of the three growth modes, as a function of the coverage θ in ML: (a) island, or Volmer-Weber growth; (b) layer-plus-island, or Stranski-Krastanov growth; (c) layer-by-layer, or Frank-van der Merwe growth (adapted from Venables et al [7] 1984)

The **Stranski-Krastanov** (or layer plus island) growth mode (Figure 1.2 (b)) is an interesting intermediate case. After forming the first monolayer (ML), or a few ML, according to the 2D layer by layer mode, subsequent layer growth is unfavorable and islands are formed over the intermediate 2D layer. There are now many examples of its occurrence in metal-metal, metal-semiconductor, gas-metal and gas-layer compound systems[1,7,12]. The phenomenon of strain-assisted self assembly in the Ge/Si(100) system is a popular example of this phenomenon today.

The distinctions of the three growth modes can be understood qualitatively in terms of the relative surface energies of crystal A (γ_A), crystal B (γ_B) and the effective interfacial energy γ^*, as illustrated in Figure 1.3. The effective interfacial energy γ^* represents the excess energy of the interfacial region above the values for bulk A and B in that region.

If the deposit is A, and the substrate is B, the condition $\gamma_A + \gamma^* < \gamma_B$ leads to layer growth, as shown in Figure 1.3 (a). The condition is therefore not satisfied if B is the deposit and A the substrate, and this leads to island growth, as illustrated in Figure 1.3 (b). However, if we have layer growth initially, then it is often the case that the effective interfacial energy γ^* increases with thickness of the layer, for example due to strain in this layer. In such a case, the thermodynamic conditions for layer growth are terminated after a certain layer thickness. Further growth of the layers is then in competition with growth of the more stable islands. This thermodynamic situation is very common, so that many crystal growth systems can be classified as Stranski-Krastanov (SK) growth.

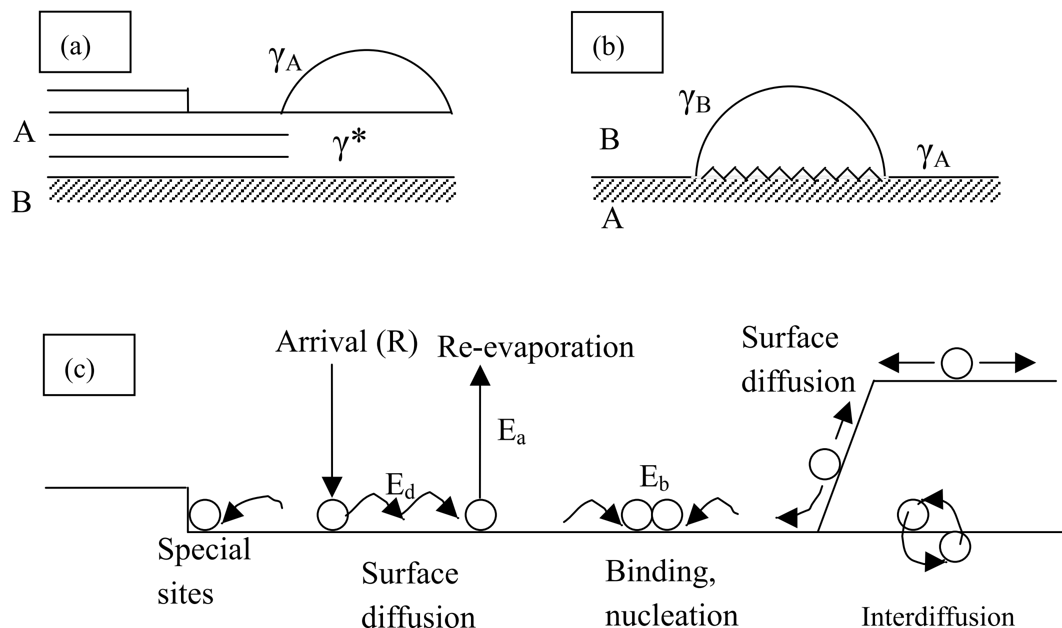

Figure 1.3 (a) Growth of A on B, where $\gamma_A < \gamma_B$; misfit dislocations are introduced, or islands after a few 2D layers have been deposited; (b) Growth of B directly onto A as islands. (c) Surface processes and characteristic energies in nucleation and film growth (adapted from Venables et al[7]).

1.1.3 Evolution of Growth

The essential atomistic features occurring during a 3-D nucleation process are illustrated in Figure 1.4. Initially the impinging flux of atomic species becomes thermally equilibrated with the substrate. If the substrate is held at a sufficiently high temperature, the atoms may diffuse over the substrate surface and interact with other adatoms; they may also re-evaporate from the surface. In the case of deposition of a single element (e.g. Cu or Ni) the formation of bonds between adatoms results in a decrease in the volume free energy, according to the relationship $4/3\pi r^3 \Delta G_v$. However, there will be a corresponding increase in free energy due to the surface area of the nucleus. Competition between the volume and surface free energies results in an initial increase in total free energy upon nucleation, characterized by a nucleation barrier ΔG*, as shown in Figure 1.5. The larger the volume free energy changes, the smaller the value of ΔG*.

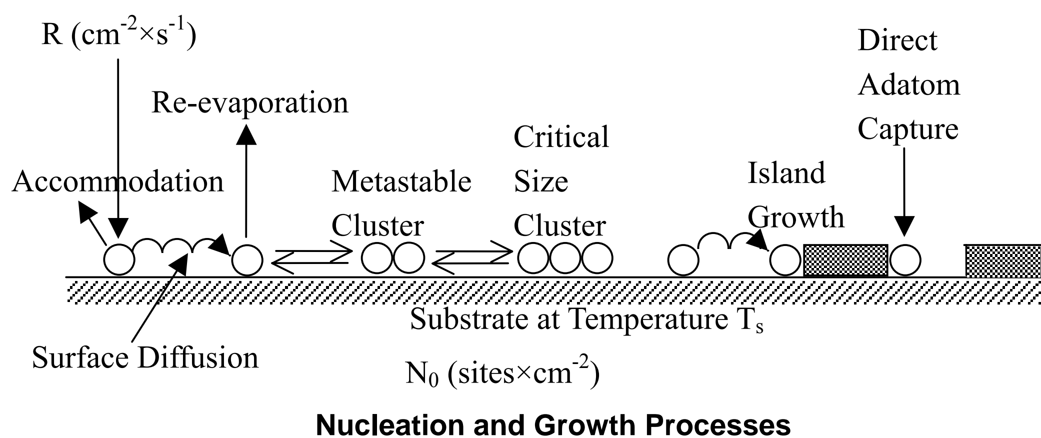

Figure 1.4 Schematic representation of processes leading to three-dimensional nucleation and film growth (adapted from Venables et al [7]).

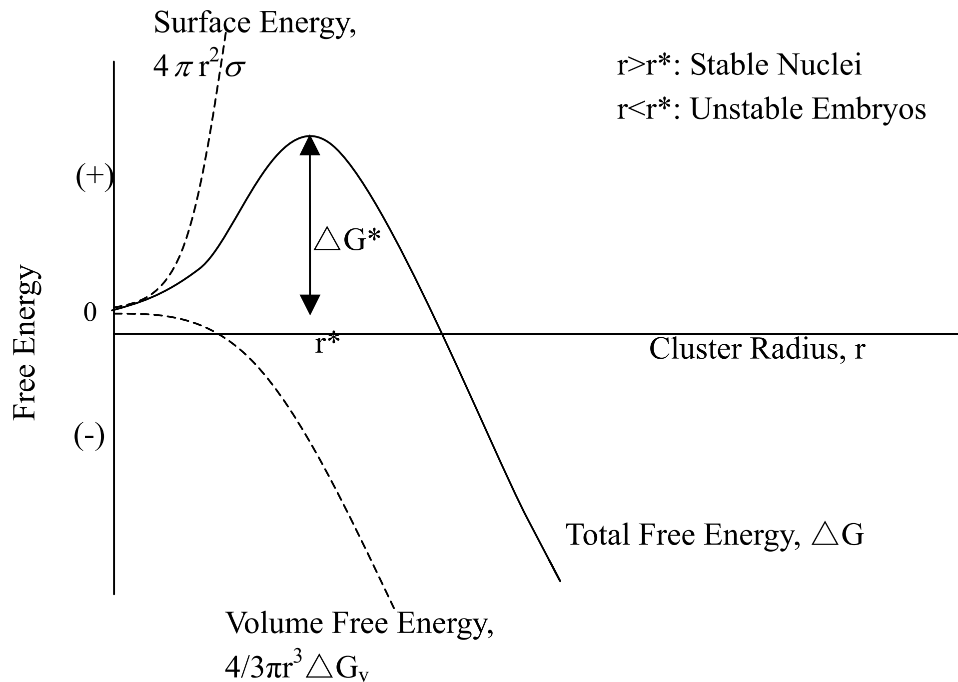

Figure 1.5 Schematic diagram showing free energy versus the radius r of a spherical nuclei (adapted from Venables et al [7]).

During the nucleation stage, where stable nuclei are formed, the number density increases with time until a *saturation nucleation density* is reached, at which point the number density will decrease due, for example, to island coalescence events. The saturation nucleation density at this primary nucleation stage increases with decreasing deposition temperature, since the adatom mobility decreases.

The nucleation density can be written in the form $n_x \sim R^p \exp(E/kT)$[10], where p is a constant, E is the activation energy for surface diffusion of the depositing species on the substrate surface, n_x is the island nuclei density, R is the deposition rate, T is the temperature (K), and k is the Boltzmann constant (1.380658×10^{-23} $J \cdot K^{-1}$).

By plotting the nucleation density (Log (N/cm^2)) as a function of 1000/T, we

can determine the activation energy for surface diffusion of the depositing material from the slope of the curve (eV).

During the subsequent coalescence process, upon contact between impinging particles (islands), a neck is formed between the particles. Through the process of self-diffusion the overall energy of the combined particles now tends towards a minimum. This may involve a reduction in the deposit:substrate interfacial area (a process we shall refer to as dewetting), and/or a filling in of the neck region between the particles. The material filling in the neck region may come from the depositing flux, material already deposited, or a combination of both.

1.2 Thin Film Deposition Techniques[13,14,15]

The thin films can be prepared by a wide variety of techniques, and most substances can be prepared in thin film form. The most common means of preparing thin films, particularly single crystal films for structural studies, is the evaporation method.

1.2.1 Evaporation Method

The most important factor is the quality of the vacuum in which the evaporation is carried out. When provided with a pressure of 10^{-5}-10^{-6} torr, the residual inert or non-condensable gases may have a big influence and could well become incorporated in the growing film. Therefore, the so-called ultra high vacuum with

pressure of 10^{-9}-10^{-11} torr is preferable in the evaporation method.

Many different techniques are used for providing the vapor sources, the most satisfactory being the electron bombardment to melt a small region of a block of the depositing material. Electron bombardment sources are the most appropriate for use in UHV systems.

The rate of deposition, and the final film thickness often need careful control, since the structure of a deposited film can depend considerably upon both parameters. The thickness can be measured by a ratemeter, or from the amount of material evaporated from the source, or measured after deposition.

It is common to heat the substrate during deposition, particularly when good epitaxy on a single crystal substrate is required. The heating can have important effects in relation to the cleaning of the substrate, as well as enhancing recrystallization effects and general structural changes during growth, which can be important for increasing grain size and removing lattice imperfections. It is particularly important to ensure that material deposited on the heater during one experiment, will not subsequently act as a source of contamination.

1.2.2 Sputtering

Another useful method of providing the source of deposit material is to bombard a target by energetic particles, so that surface atoms are ejected and can be condensed onto a substrate to form a film. There are two kinds of sputtering: cathodic

sputtering and reactive sputtering.

One of the main differences in the mode of growth of sputtered deposits, in comparison with evaporated deposits, is that the depositing atoms can have very much higher kinetic energy. This may be sufficient to allow depositing atoms to penetrate the substrate surface, and means that the sputtered deposit atoms can have a very high initial surface mobility. Therefore, the sputtered deposits are expected to have structural characteristics equivalent to those formed by the evaporation technique on substrates at higher temperatures.

1.2.3 MBE

Molecular Beam Epitaxy (MBE) is a versatile technique for growing thin epitaxial structures made of semiconductors, metals or insulators. MBE offers significantly more precise control of the beam fluxes and growth conditions. Because of vacuum deposition, MBE growth is carried out under conditions far from thermodynamic equilibrium and is governed mainly by the kinetics of the surface processes occurring when the impinging beams react with the outermost atomic layers of the substrate crystal.

As MBE is realized in an ultrahigh vacuum environment, growth could be controlled *in situ* by surface diagnostic methods such RHEED, AES, ellipsometry or optical reflectance-difference and laser interferometric methods.

1.3 Ni and MgO

MgO is an electrical insulator exhibiting the NaCl structure[16] with the space group of $Fm\bar{3}m$. It has a lattice parameter of 4.2042Å at room temperature. Ni is an *fcc* (face-centered cubic) transition metal exhibiting ferromagnetic properties and the same space group as MgO. The lattice parameter of Ni is 3.5238Å at room temperature, and thus the lattice mismatch between Ni and MgO at this temperature is 16.18%.

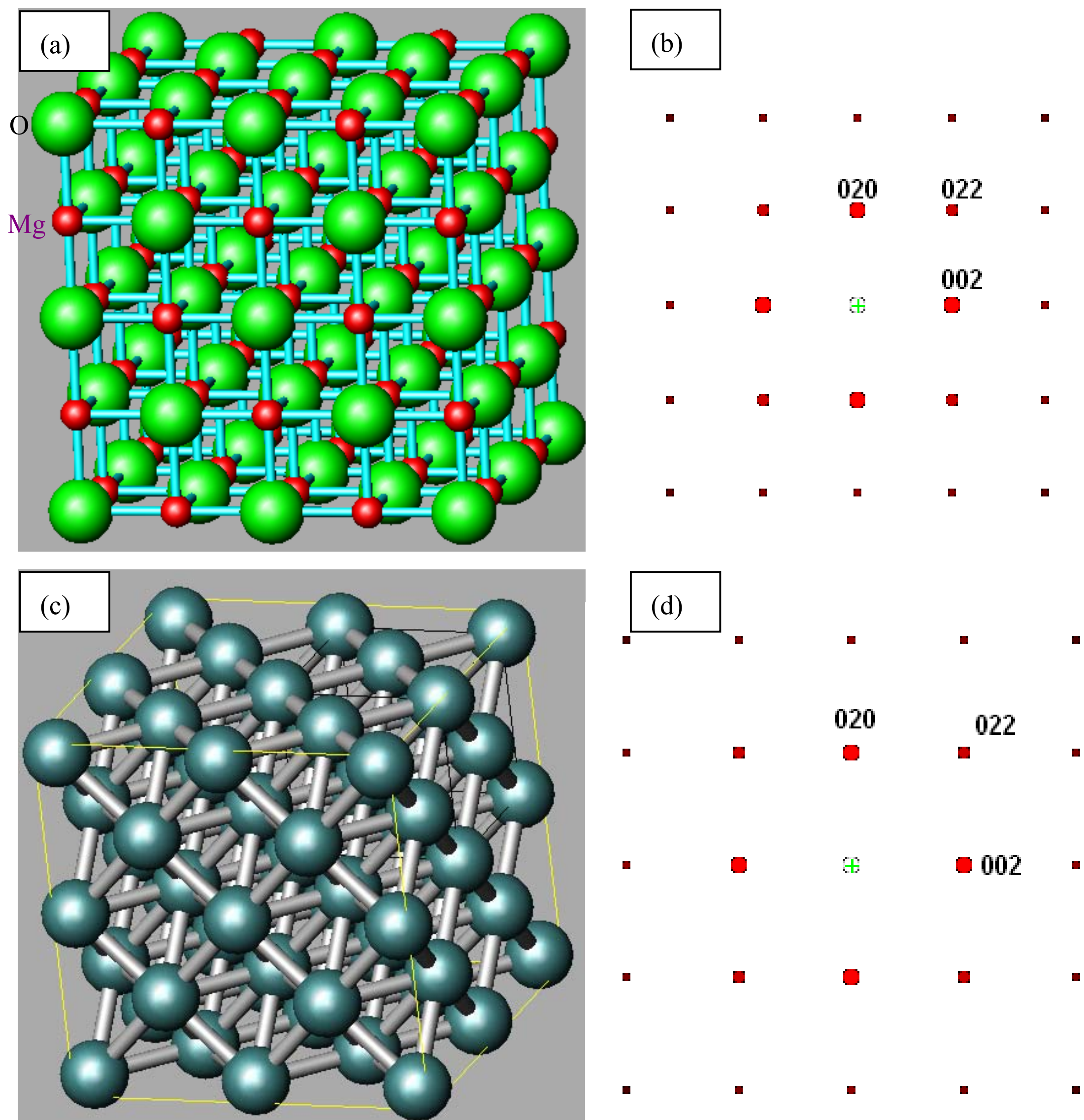

Figure 1.6 (a) Solid state structure of MgO; (b) Simulated <100> orientation diffraction pattern of MgO (001); (c) Solid state structure of Ni; (d) simulated <100> orientation diffraction pattern of Ni (001), of the same camera length with (b).

The thermal expansion coefficient of MgO as a function of temperature is presented in Figure 1.7, after Kingery et al[17]. The thermal expansion coefficient for Ni is of the form[18]:

$$\Delta L/L_0=1.362\times10^{-5}(T-293)+4.544\times10^{-7}(T-293)^2-1.806\times10^{-10}(T-293)^3 \quad (293<T<895)$$

As temperature is increased, the lattice mismatch between Ni and MgO increases. At a temperature of 550ºC (the highest growth temperature employed in this work), a_{Ni}= 3.5527Å and a_{MgO}= 4.2950Å, giving a lattice mismatch of 17.28%.

There is almost no influence of temperature on the surface energy of MgO substrate[19]. In the case of metals, the surface free energy at temperature T, below the melting point (T_m) can be estimated by the empirical rule[20]:

$$\gamma(T)=1.2\gamma_m+4.5\times10^{-4}(T_m-T),$$

where γ_m is the liquid-metal surface energy at the melting point (T_m).

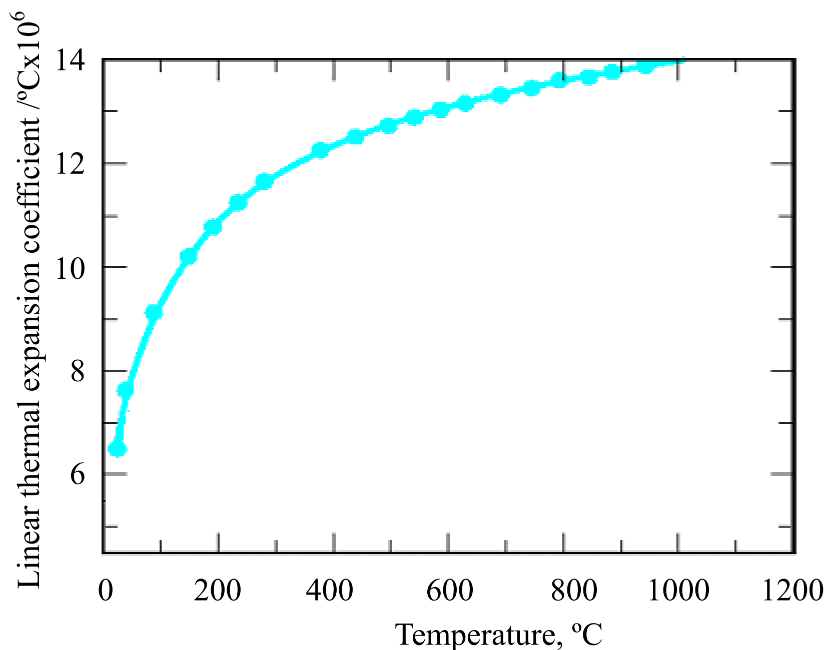

Figure 1.7 Thermal expansion coefficient of MgO

1.4 Magnetic properties of thin films

---------Magneto-optical Kerr effect (MOKE)

1.4.1 Introduction[21]

The motivation of the present work is concerned with the magnetic properties of thin film, and their application in data storage technologies. Therefore, a technique for probing the magnetic properties of the films is of critical importance.

The magneto-optical Kerr-effect refers to the dependence of the polarization state of light reflected from ferromagnetic surfaces on the magnetization state of that surface. The phenomenon has been used for many years to observe magnetic domains at bulk magnetic surfaces. Bader et al[22] noted the ease with which hysteresis loops could be determined from ultrathin films; this effect, now called the *surface magneto-optical Kerr effect* (SMOKE), has found wide application for the study of magnetism in ultrathin films as thin as a single monolayer. An excellent review has been given by Liu and Bader[23].

The SMOKE signals obtained during the experiments appear to be proportional to the magnetic moment of the ultrathin film. However, strongly nonlinear dependence on film thickness has been reported by Weller et al[24] for NdFeCo films, with a maximum of the Kerr-rotation at 2nm film thickness, with zero signal at 4nm. The effect therefore cannot be taken generally as a direct measure of magnetic moment. Its strong merit is the easy application in UHV and ready combination with other thin-film

and surface techniques. A schematic diagram illustrating the various geometries by which the SMOKE technique can be used to determine the magnetization M of a film is presented in Figure 1.8.

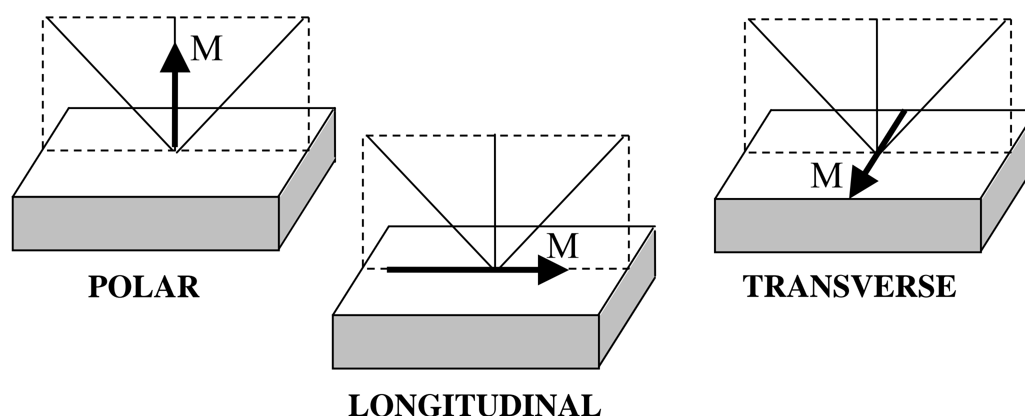

Figure 1.8 The orientation of the magnetization with respect to the scattering plane for each of the three principle geometries for the Kerr effect. The polar and longitudinal geometries describe the magnetization M in the scattering plane, normal and parallel to the sample surface respectively. The transverse (equatorial) geometry describes the case where the magnetization is perpendicular to the scattering plane but in the plane of the sample surface.

The magneto-optic Kerr effect can be described as the magnetization-induced change in polarization state and/or intensity of the light reflected from the surface of a magnetized medium.

At normal incidence, the plane of polarization of light is found to be rotated, and is known as the polar Kerr effect. The amount of rotation in the case of saturated ferromagnetic transition metals is a sizeable fraction of a degree, and therefore easily measurable.

Using a relatively simple arrangement, the effect was first demonstrated by reflecting light from the polished poles of an electromagnet. Since light penetrates metals only a short distance, determined by the optical skin depth (typically 15-20nm in metals), ultrathin films can yield a measurable Kerr rotation.

The origin of magneto-optical effects in ferromagnetic metals lies in the spin-orbit interaction between the electron spin and the orbital angular momentum. The electric field of incident light couples to the electron dipoles via the orbital wave functions which are in turn influenced by the electron spin via the spin-orbit interaction. In ferromagnets a net electron spin polarization leads to an overall rotation of the polarization of the light. Calculation of the magneto-optic response of metals requires that the spin-resolved bandstructure is known. Spin dependent optical transitions are calculated for the appropriate photon energy for right and left circularly polarized light. For the ferromagnetic transition metals, for example, the magneto-optic contribution to the conductivity (off-diagonal components of the conductivity tensor) has been computed in the visible range. Since the electronic structure of films beneath typically 5ML thickness may show departures from the bulk structure, the magneto-optic response is modified accordingly. Surprisingly, bulk constants do appear to describe well experimental measurements of Kerr spectra obtained for Fe/Ag[25] films only a few monolayers in thickness, but studies for Co/Au films[26] show that an interface-induced Kerr rotation exists. Experiments on Fe/Au/Fe and Fe/Ag/Fe trilayer structures[27] have confirmed the presence of new optical

transitions associated with spin polarized quantum well states confined to the non-magnetic spacer layers. Following recent advances in computational and measurement techniques, it may soon be possible to obtain accurate agreement between measured and calculated magneto-optic constants. Thus magneto-optical studies of ultrathin films may soon be placed on a more quantitative footing.

1.5 *In-situ* Transmission Electron Microscopy

In-situ electron microscopy was originated by Bassett[28] and extended by Pashley[29]. The applications of this technique were confined to simple systems considered least susceptible to contamination effects (such as oxidation) and began with the growth of noble metals on molybdenite. Pashley[30] suggested changing the strategy from in-depth studies of a very restricted class of systems to balanced studies of a broader variety of systems.

It is widely known that specimens in the electron microscope subject to conventional high vacuum conditions (~10^{-6}Torr) tend to suffer substantial carbonaceous contamination resulting from electron bombardment of residual hydrocarbons (Ennos 1953[31], 1954[32]). The construction of ultrahigh vacuum electron microscopes, with chamber pressures in the range 10^{-9}-10^{-10}Torr was then attempted by a number of workers with limited success. It was not until the late 1980's that instruments began to appear exhibiting stable UHV conditions at the sample location.

The most common designs for achieving UHV performance in the TEM

employ a system of differential pumping apertures. Using these systems, pressures of at least two orders of magnitude may be sustained between the sample chamber and the remainder of the electron column (the electron gun and camera chamber).

To achieve base pressures in the region of 10^{-10}Torr, all the components sharing the vacuum must be bakeable to in excess of 100ºC, to remove adsorbed water vapor from the interior surfaces of the vacuum chamber[33]. Polymer-based vacuum seals are avoided due to outgassing and the need for baking. Low-oxygen copper seals are typically employed.

References:

[1] R. Beanland, C. J. Kiely and R. C. Pond, in: *Handbook on Semiconductors*, (Amsterdam; New York: North-Holland, 1992-1994).
[2] J. W. Matthews, Phil. Mag., 13, 1207 (1966).
[3] J. W. Matthews, Acta. Metallogr., 15, 595 (1967).
[4] D. W. Pashley, M. J. Stowell, M. H. Jacobs and T. J. Law, Phil. Mag., 10, 127 (1964).
[5] R. Kern, G. L. Lay and J. J. Metois, in: *Current Topics in Materials Science*, (North-Holland, Amsterdam, 1979).
[6] G. Honjo and K. Yagi, in: *Current Topics in Materials Science*, (North-Holland, 1980).
[7] J. A. Venables, G. D. T. Spiller and M. Hanbucken, Rep. Prog. Phys., 47, 399 (1984).
[8] J. E. Greene, in: *Deposition Technologies for Films and Coatings*, (Noyes Publications, Park Ridge, 1994).
[9] A. Zangwill, *Physics at surfaces*, (Cambridge University Press, Cambridge, 1988).
[10] E. S. Machlin, in: *Materials Science in Microelectronics*, (Giro Press, New York, 1995).
[11] P. B. Barna and M. Adamik, in: *Science and Technology of Thin Film*, (World Scientific Publishing Co., Singapore, 1995).
[12] J. A. Venables, *Introduction to Surface and Thin Film Processes*, (New York : Cambridge University Press, 2000).
[13] D. W. Pashley, Adv. Phys., 14, 327 (1965).
[14] O' Hanlon, J. Vac. Sci. Technol. A, 12, 921 (1994).
[15] J. O. Carlsson, in: *Handbook of Deposition Technologies for Films and Coatings*, (2nd Edn, Noyes Publications, 1991).
[16] H. Fornander, L. Hultman, J. Birch and J. E. Sundgren, J. Cryst. Growth., 186, 189 (1998).
[17] W. D. Kingery, H. K. Bowen and D. R. Uhlmann, *Introduction to Ceramics*, (2nd Edn., John Wiley & Sons, Inc., New York, 1976).
[18] D. R. Lide (Ed.), *CRC Handbook of Chemistry and Physics*, (73rd Edn., CRC Press, Boca Raton, FL, 1992-1993).
[19] J. J. Gilman, J. Appl. Phys., 31, 2208 (1960).
[20] L. E. Murr, in: *Interfacial Phenomena in Metals and Alloys*, (Addison-Wesley, Reading, MA, 1975).
[21] J. A. C. Bland, *Polarized Electron/Polarized Photon Physics*, (Plenum Press, New York, 1995).
[22] S. D. Bader, E. R. Moog and P. Gruenberg, J. Magn. Magn. Mater., 53, 295 (1986).
[23] C. Liu and S. D. Bader, J. Magn. Magn. Mater., 93, 307 (1991).
[24] D. Weller, W. Reim and P. Schrijner, IEEE T Magn., 24, 2554 (1988).
[25] Z. Q. Qiu, J. Pearson and S. D. Bader, Phys. Rev. B, 45, 7211 (1992).
[26] S. Visnovsky, M. Nyvlt, V. Prosser, J. Ferré, G. Pénnisard, D. Renard and G. Sczigel, J. Magn. Magn. Mater., 128, 179 (1993).
[27] T. Katayama, Y. Suzuki, H. Hayshi and A. Thiaville, J. Magn. Magn. Mater., 126, 527 (1993).
[28] G. A. Bassett, *Proc. Eur. Reg. Conf. Electron Microscopy*, (Delft,1960).
[29] D. W. Pashley, Adv. Phys., 14, 372 (1965).
[30] D. W. Pashley, *Epitaxial Growth*, (New York, San Francisco, London: Academic,

1975).
[31] A. E. Ennos, Br. J. Appl. Phys., 4, 101 (1953).
[32] A. E. Ennos, Br. J. Appl. Phys., 5, 27 (1954).
[33] M. Yeadon, in: *Encyclopaedia of Nanoscience and Nanotechnology*, (American Scientific Publishers, Stevenson Ranch CA, 2003).

CHAPTER 2 Literature Review

Metal-ceramic interfaces are important in applications as diverse as magnetic storage media and support catalysts. It is very important to understand how the crystallography and microstructure of metallic films deposited onto ceramic substrates depend on growth and /or annealing conditions so that their physical properties (e.g. their magnetic and electronic properties) can be tailored for specific applications. To this end, we have studied the epitaxial growth of Ni films deposited by electron beam evaporation onto MgO (001) substrates. Using a novel UHV *in-situ* TEM we have observed directly the evolution of the film microstructure as a function of time and growth temperature.

There are a few published papers on the subject of the growth of Ni on MgO(100), and we begin with a discussion of this prior work. We then briefly review the subject of *in-situ* electron microscopy.

2.1 Previous Studies of Ni on MgO

There are some factors that can influence the epitaxial growth of Ni on MgO (001) substrates, such as lattice mismatch, deposited film thickness, growth temperature and annealing.

2.1.1 Lattice Mismatch

Honjo and Yagi[1,2] studied a variety of metal films including Ni, Pd, Cu, Pt,Al,

Fe, Ag and Au deposited on MgO (001) substrates in an *in-situ* UHV TEM chamber, establishing the epitaxial relationship with the lattice parameter ratio ρ. The relations found for three series of materials, alkali halides and chalcogenide compounds of the NaCl type structure and iron, indium and *fcc* metals, deposited on the (001) MgO are summarized in Figure 2.1 with respect to the values of the lattice parameter ratio, $\rho=a_d/a_s$, of the deposits and the substrate MgO. When $\rho=a_{Ni}/a_{MgO}=0.8385$, according to the map, we found two epitaxial orientations exist: $(001)_{Ni}//(001)_{MgO}$, $[100]_{Ni}//[100]_{MgO}$ and $(1\bar{1}0)_{Ni}//(001)_{MgO}$, $[11\bar{2}]_{Ni}//[100]_{MgO}$, among which the latter orientation is preferable. In contrast to our experiments, Honjo and Yagi did not observe any *hcp* phases, nor transitions between different orientations.

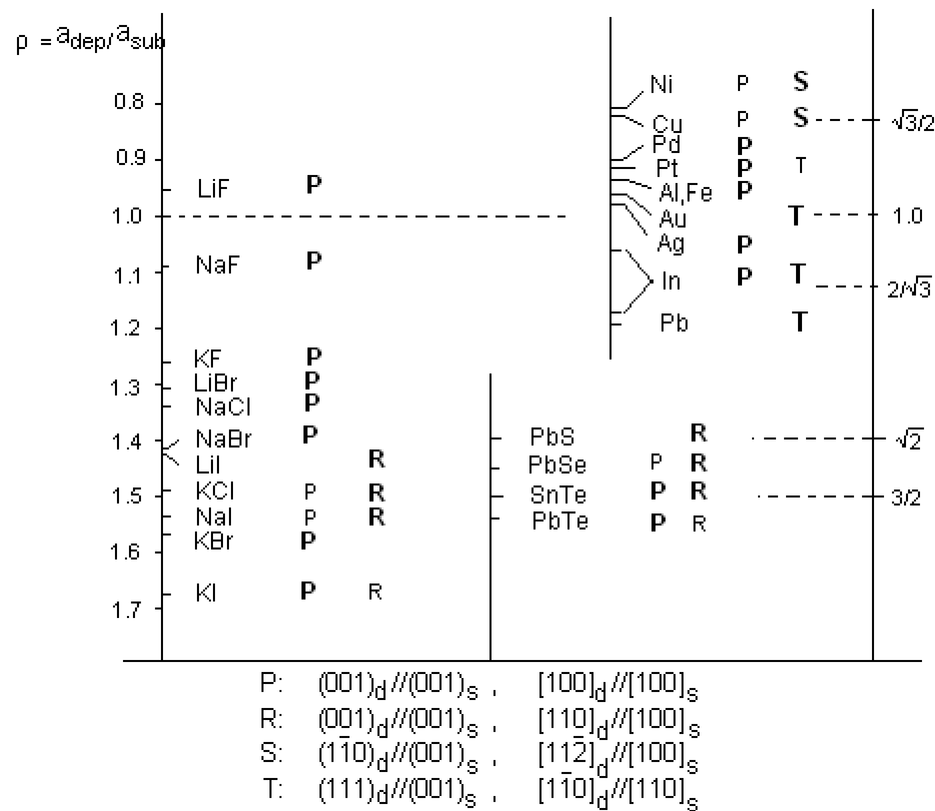

Figure 2.1 Epitaxial orientations of alkali halides, chalcogenide compounds and metals on (001)MgO with reference to the lattice parameter ratio $\rho=a_d/a_s$ (d:deposit and s:substrate). The sizes of the orientation symbols roughly represent relative preferences.

2.1.2 Film Thickness

Raatz and Woltersdorf[3] observed a strong dependence of the film orientation on film thickness. According to their experiments (on films approaching 20nm thickness), the orientation Ni(001)//MgO(001) and Ni<100>//MgO<100> are formed under the following conditions:

$T_s=400^o$ C, $d_{Ni}<50$nm,

$T_s=500^o$ C, $d_{Ni}<40$nm,

$T_s=600^o$ C, $d_{Ni}<25$nm.

With increasing deposited thickness, recrystallization processes become even more predominant within the monocrystalline (001) epitaxial layers, resulting in the occurrence of regions with (110) orientation. Two equivalent possibilities can be distinguished: (110)Ni//(001)MgO; $[1\bar{1}1]$Ni//[010]MgO and (110)Ni//(001)MgO; $[1\bar{1}1]$Ni//[100]MgO.

Ni films containing (110)-oriented regions were observed under the conditions:

$T_s=400^o$ C, $d_{Ni}=50$ to 65nm,

$T_s=500^o$ C, $d_{Ni}=40$ to 50nm,

$T_s=600^o$ C, $d_{Ni}=25$ to 30nm.

Reorientation processes within the Ni layers were found to have taken place within a relatively narrow thickness range. At thicknesses above this range where the (110) material is stable, the film was found to reorient to the cube-on-cube (100) orientation.

2.1.3 Growth Temperature

McCaffrey et al[4] studied the epitaxial Ni films deposited on (001) MgO under different growth temperatures by DC magnetron sputtering under ultrahigh vacuum conditions. Cube on cube orientation was predominantly observed at 100ºC by Qiu et al[5,6]; while Ni $[75\bar{1}]$ // MgO [001] and Ni $(\bar{1}1\bar{2})$ // MgO (100) was found at the higher temperature of 400º C. The new epitaxial relationship reduced the lattice mismatch between the deposit and the substrate from 16% to 1.6% and 2.5% in the two different directions respectively. This may occur through dislocation motion to relieve strain[7] (the film may find states of lower free energy when dislocation movement to interface reduces strain[8,9]), or strictly through nucleation and growth processes[10], or a combination of these.

Svedberg et al[10] also studied the growth of Ni films by DC magnetron sputtering onto MgO (100) substrates with temperatures ranging from 20 to 700ºC for 200 nm thick films. At a reduced temperature, 20ºC, they observed a complex polycrystalline texture dominated by <220> orientated grains co-existing with $\langle 1\bar{4}1 \rangle$ and <200> texture. And at 100~200ºC, the increase in deposition temperature allows the initial nucleated Ni islands to rearrange to a single crystal <200> texture. However, at an increased temperature above 300ºC, with higher atom mobility, the Ni grew with a $\langle 75\bar{1} \rangle$ texture that both accommodated the strong Ni metal-metal bond and placed each interfacial Ni atom in a preferred position on the MgO unit cells, accommodating the mismatch better between the two crystal lattices. They calculated the coincidence

of reciprocal lattice points[11] and found $\langle 75\bar{1} \rangle$ has a larger intersecting volume than $\langle 200 \rangle$ texture, thus indicating that $\langle 75\bar{1} \rangle$ lowers the overall misfit and the interfacial energy, in addition to accommodating the preferred atomic configuration at the interface.

Michelini et al[12] deposited permalloy ($Ni_{80}Fe_{20}$) thin films on MgO (001) single crystals by a DC magnetron sputter technique in an ultrahigh vacuum chamber. The lattice mismatch between them is 17%. With the growth temperature ranging from 200ºC to 800ºC, an *fcc* structure with (001) surface is observed, and the cube on cube epitaxial relationship is maintained despite the large lattice mismatch value.

Epitaxial growth is observed with substrate temperature T_s>200° C, in all cases the epitaxial orientation was found to be (100)Ni//(100)MgO and [001]Ni//[001]MgO[13,14]. Reniers et al[14] verified that the growth of Ni on MgO (001) at room temperature (RT) is polycrystalline, while Barbier et al[15] found a stable cube on cube epitaxial relationship together with different Ni(110)//MgO(001) orientations when deposited at RT.

2.1.4 Annealing

Lukaszew et al[16] studied the structure of Ni thin film on MgO (001) grown in an MBE VG 80M system under ultrahigh vacuum by *in-situ* RHEED. The Ni RHEED pattern evolved from wide and diffuse streaks at the beginning of the growth into sharper and spotty streaks indicating three-dimensional growth. After annealing at

573K, a (2×1) surface reconstruction was evident as shown by the presence of half-order streaks. Because of the oxygen contamination of the surface, the oxygen atoms surrounded the top Ni atoms, preventing the formation of a complete top Ni layer, leading to a missing-row type surface reconstruction.

2.2 Magnetic Properties

Lukaszew et al[17,18] also studied the magnetic properties of Ni thin films on MgO single crystal substrate using longitudinal MOKE. They performed measurements on annealed and nonannealed films, and found both exhibit the expected fourfold symmetry. However, annealed films were observed to exhibit an additional uniaxial anisotropy superimposed on the usual fourfold anisotropy.

Michelini et al[19] studied the magnetic properties of the permalloy ($Ni_{80}Fe_{20}$) thin films on MgO single crystal substrate, and found both growth temperature and film thickness to influence the crystalline and magnetic properties. They reported that in all thicknesses from 35Å to 1000Å at 300ºC, the coercive field is lower than $5O_e$; while for films deposited at 600ºC, the coercive field increases with the growth temperature, up to $500O_e$. In this case, the influence of the layer thickness on their magnetic behavior is negligible compared to the deposition temperature.

Choi et al[20] studied the magnetic properties of Fe thin films on Pd (111). In this case, films were deposited at room temperature, then annealed at different temperatures before performing MOKE measurements. No hysteresis was observed for

either longitudinal or polar directions, but upon annealing at 450K, hysteresis was observed. Annealing at 600K destroyed the hysteresis loop.

In the case of annealing at 450K, a flat surface with a sharp interface could be achieved and magnetizations both in longitudinal and polar directions were concurrently induced; further annealing at 600K completely demagnetized the film.

Wang et al[21] studied the magnetic properties of Fe-Co nanoparticles and observed coercivity both in the as-prepared condition, and after annealing at 400° C, 600° C, 800° C. In this case, coercivity was dependant not only on particle size, but also the shape and packing of the particles. A large saturation magnetization (M_s) was detected for the as-prepared particles, together with a low value of the coercivity (H_c).

When annealed at 400° C, a significant increase in H_c was observed, with a corresponding decrease in M_s. Annealing at higher temperatures led to an increase in M_s and a decrease in H_c.

Shen et al[22] studied the effect of annealing on morphology and magnetic properties of ultrathin Ni films deposited on Cu (100) and demonstrated that annealing led to smoother surface morphology, with little change in the perpendicular magnetization. They concluded that perpendicular magnetization does not originate from the morphology effects, consistent with an FMR study[23].

References:

[1] G. Honjo and K. Yagi, in: *Current Topics in Materials Science*, (North-Holland, 1980).
[2] K. Takayanagi, K. Yagi and G. Honjo, Thin Solid Films, 48, 137 (1978).
[3] G. Raatz and J. Woltersdorf, Phys. Stat. Sol. (a), 113, 131 (1989).
[4] J. P. McCaffrey, E. B. Svedberg, J. R. Phillips and L. D. Madsen, J. Cryst. Growth, 200, 498 (1999).
[5] H. Qiu, H. Nakai, M. Hashimoto, G. Safran, M. Adamik, P. B. Barna and E. Yagi, J. Vac. Sci. Technol. A, 12, 2855 (1994).
[6] H. Nakai, H. Qiu, M. Adamik, G. Safran, P. B. Barna and M. Hashimoto, Thin Solid Films, 263, 159 (1995).
[7] J. C. A. Huang and C. P. Flynn, Philos. Mag. Lett., 64, 71 (1991).
[8] J. W. Matthews, J. Vac. Sci. Technol., 12, 126 (1975).
[9] B. W. Dodson and J. Y. Tsao, Appl. Phys. Lett., 51, 1325 (1987).
[10] E. B. Svedberg, P. Sandström, J. E. Sundgren, L. D. Madsen and J. E. Greene, Surf. Sci., 429, 206 (1999).
[11] S. Stemmer, P. Pirouz, Y. Ikuhara and R. F. Davis, Phys. Rev. Lett., 77, 1797 (1996).
[12] F. Michelini, L. Ressier and J. Degauque, J. Appl. Phys., 92, 7337 (2002).
[13] H. Bialas and K. Heneka, Vacuum, 45, 79 (1994).
[14] F. Reniers, M. P. Delplancke, A. Asskali, V. Rooryck and O. V. Sinay, Appl. Surf. Sci., 92, 35 (1996).
[15] A. Barbier, G. Renaud and O. Robach, J. Appl. Phys., 84, 4259 (1998).
[16] R. A. Lukaszew, V. Stoica, C. Uher and R. Clarke, Mat. Res. Soc. Symp. Proc., 648, P3.29.1 (2001).
[17] R. A. Lukaszew, Z. Zhang, V. Stoica and R. Clarke, Appl. Surf. Sci., 219, 74 (2003).
[18] R. A. Lukaszew, Z. Zhang, C. Cionca, V. Stoica, and R. Clarke, J. Vac. Sci. Technol. A, 21, 1524 (2003).
[19] F. Michelini, J. Degauque, P. Baulès, J. P. Peyrade, J. L. Gauffier and J. F. Bobo, J. Magn. Magn. Mater., 242, 173 (2002).
[20] J. H. Choi, T. U. Nahm, W. Kim, W. Kim, J. Chung, J. Y. Kim and S. J. Oh, Surf. Sci., 495, 173 (2001).
[21] Z. H. Wang, C. J. Choi, B. K. Kim and Z. D. Zhang, J. Alloys and Compounds, 351, 319 (2003).
[22] J. Shen, M. T. Lin, J. Giergiel, C. Schmidthals, M. Zharnikov, C. M. Schneider and J. Kirschner, J. Magn. Magn. Mater., 156, 104 (1996).
[23] B. Schulz and K. Baberschke, Phys. Rev. B, 50, 13467 (1994).

CHAPTER 3 Experiment

All experiments were performed under an ultrahigh vacuum *in-situ* transmission electron microscope (UHV TEM), with real time observations of the growth of Ni islands on the MgO surface made using bright field and dark field imaging techniques. The crystallographic orientations of the islands were determined from electron diffraction patterns, and the physical properties explored using an *ex-situ* MOKE (Magneto-Optical Kerr Effect) system.

The advantage of the *in-situ* TEM system lies in the fact that both real space and reciprocal space lattice information from the same selected area of the sample can be observed, and microstructural developments monitored as a function of deposition time.

3.1 Principles of Transmission Electron Microscopy

The TEM is a very powerful and versatile instrument that is capable of characterizing the internal structure of materials. The electron beam in the TEM is oriented normal to the plane of the sample, penetrates the sample, and generates an image or diffraction pattern in the forward direction. High energy electron beams (~100-300keV per electron) and very thin samples (~10-1000Å) are typically employed.

TEM allows us to:

(1) Image microstructure, e.g. looking at nanomaterials.

(2) Identify phases present either by electron diffraction or chemical analysis techniques such as electron energy loss spectroscopy (EELS).

(3) Analyze defects, e.g. dislocations and stacking faults.

(4) Analyze the orientation of buried interfaces, e.g. epitaxial orientation relationships.

3.1.1 Optical System

The TEM is a broad-beam instrument as compared with a scanned probe instrument such as the scanning electron microscope. A typical electron optical column comprises a set of condenser lenses, an objective lens, an intermediate lens system and finally a projector lens.

A schematic diagram of a typical TEM column is presented in Figure 3.1, where CL1, 2 is the first condenser lens (double gap), and CL3 is the second condenser lens, its function being to converge the beam at the specimen and control the diameter of the illuminated area of the specimen. The condenser aperture, CL aperture increases resolution but degrades intensity.[1]

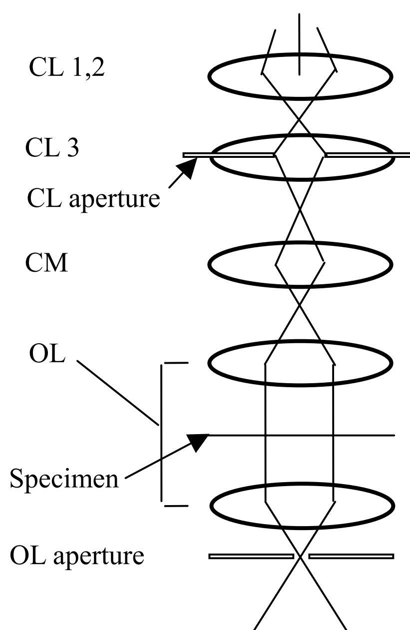

Figure 3.1 TEM illumination system

The objective lens, OL, forms an inverted initial image, which is subsequently magnified. Both the diffracted and unscattered electrons are focused by the objective lens. A diffraction pattern is formed at the back focal plane of the objective lens. The specimen sits between a pair of lenses forming the objective. The objective aperture is placed in the back focal plane of the objective lens. Its function is to select those electrons which will contribute to the image, excluding diffuse scatter, thereby improving the contrast of the final image[1].

3.1.2 Selected-area Diffraction

By focusing the intermediate lens (and hence subsequent lenses) on the back focal plane of the objective lens, a diffraction pattern may be formed on the viewing screen. This pattern contains valuable information about the crystallographic structure

and lattice spacing of the sample. A schematic diagram of a diffraction pattern is presented in Figure 3.2.

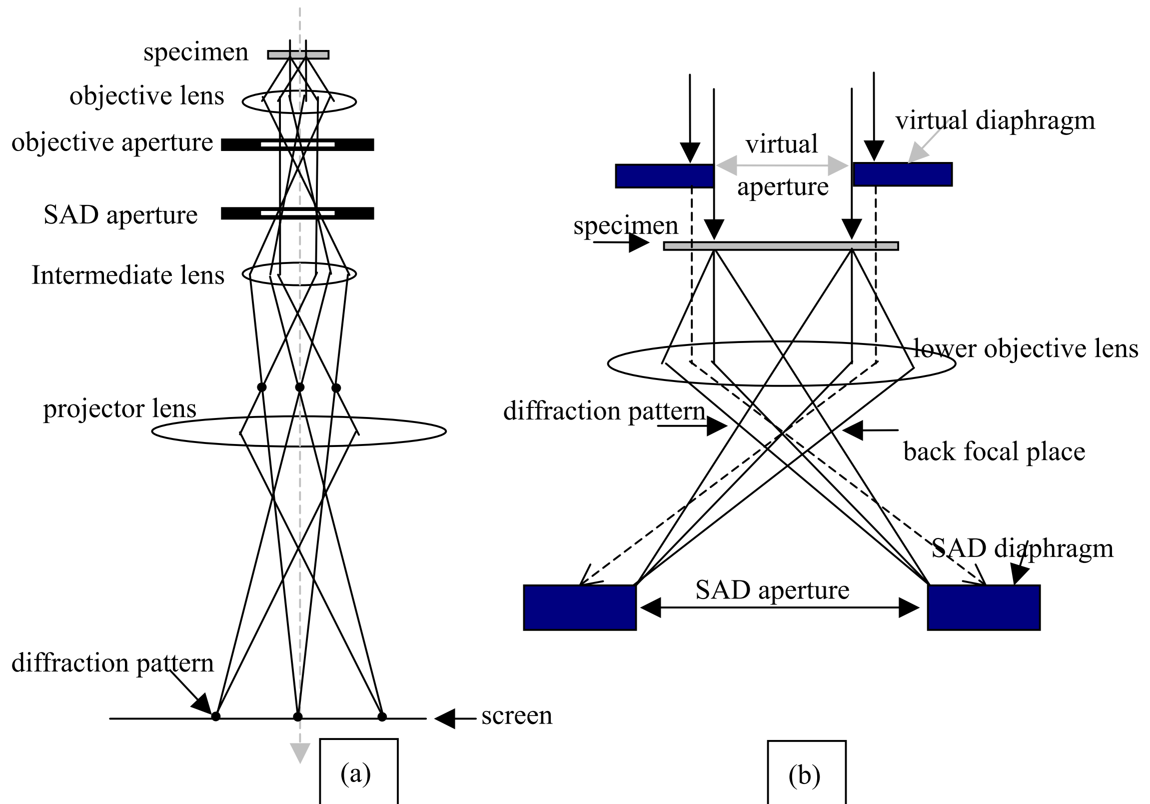

Figure 3.2 Schematic of diffraction pattern and SAD pattern (adapted from reference [1]), (a) projecting the diffraction pattern on the viewing screen; (b) showing SAD pattern formation: the insertion of an aperture in the image plane results in the creation of a virtual aperture in the plane of the specimen, only electrons falling inside the dimensions of the virtual aperture at the specimen will be allowed through into the imaging system, all other electrons will hit the SAD diaphragm.

The spacings between the central bright spot (the direct beam) and the other reflections correspond to the interplanar spacings of the planes matching those reflections.

An expression relating the spacings measured from the photographic plate (e.g. using a ruler) and the crystal lattice is readily derived.

From the Bragg equation: $n\lambda=2d\sin\theta$, where n is the order of diffraction, λ is the

electron wavelength, d is the interplanar spacing and θ the Bragg angle. From Figure 3.3, spot A is from the first zone, so the Bragg equation can be written as $\lambda=2d\theta$---(1), assuming θ to be small.

From Figure 3.3, $\tan(2\theta)=R/L$, where R is the measured distance on the plate between the direct beam and the diffracted beam and L is the camera length (effective distance between the specimen and photographic plate in the TEM). As the angle θ is quite small, we can write the equation as $2\theta=R/L$ ---(2).

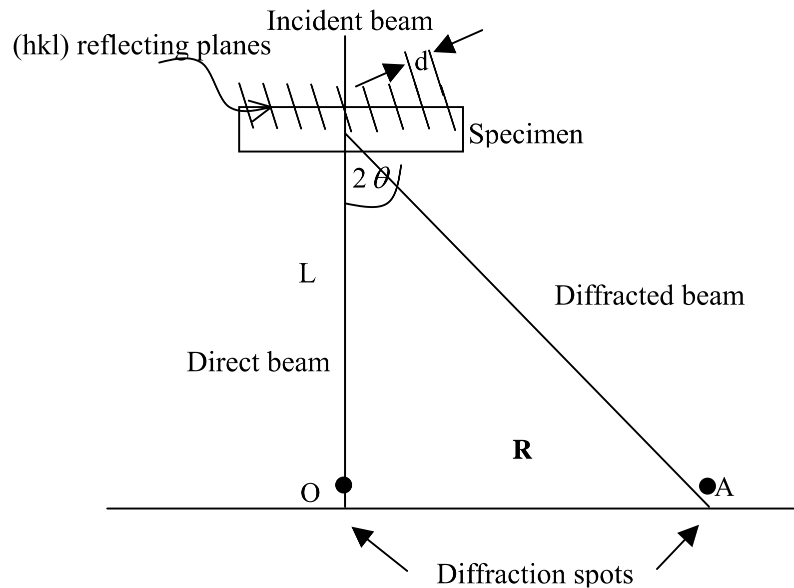

Figure 3.3 The relationship between the spacing R of diffraction maxima and camera length,L.

Combining equations (1) and (2), we obtain $\lambda L=Rd$[1] ---(3) which is the fundamental relationship in a diffraction pattern.

3.1.3 Bright field and Dark field imaging

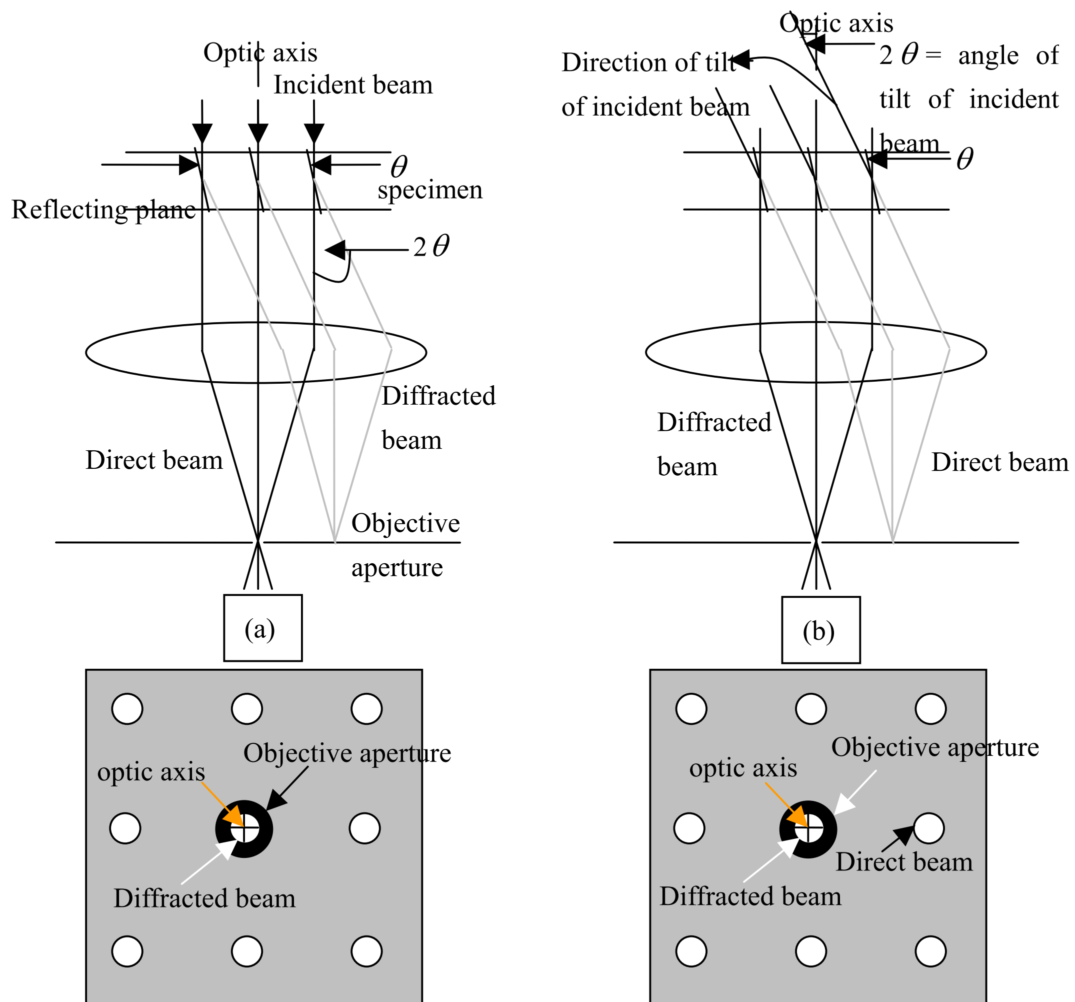

Figure 3.4 Ray diagrams showing how the objective lens/aperture are used in combination to produce (a) a BF image formed from the direct beam, and (b) a CDF image where the incident beam is tilted so that the scattered beam remains on axis. The area selected by the objective aperture, as seen on the viewing screen, is shown below each ray diagram. (adapted from reference [1])

When the SAD pattern is projected onto the viewing screen, we can use the pattern to perform the two most basic imaging operations in the TEM. The pattern contains a bright central spot which contains the direct electrons and some scattered electrons. If the direct beam is selected as shown in Figure 3.4 (a), we call the resultant

image a bright-field (BF) image. If the beam tilt above the objective lens adjusted, the incident beam hits the specimen at an angle equal and opposite to the scattering angle. In this way the scattered electrons will now travel down the optic axis, as shown in Figure 3.4 (b). This operation is called centered dark-field (CDF) imaging.

3.2 Introduction of MERLION system

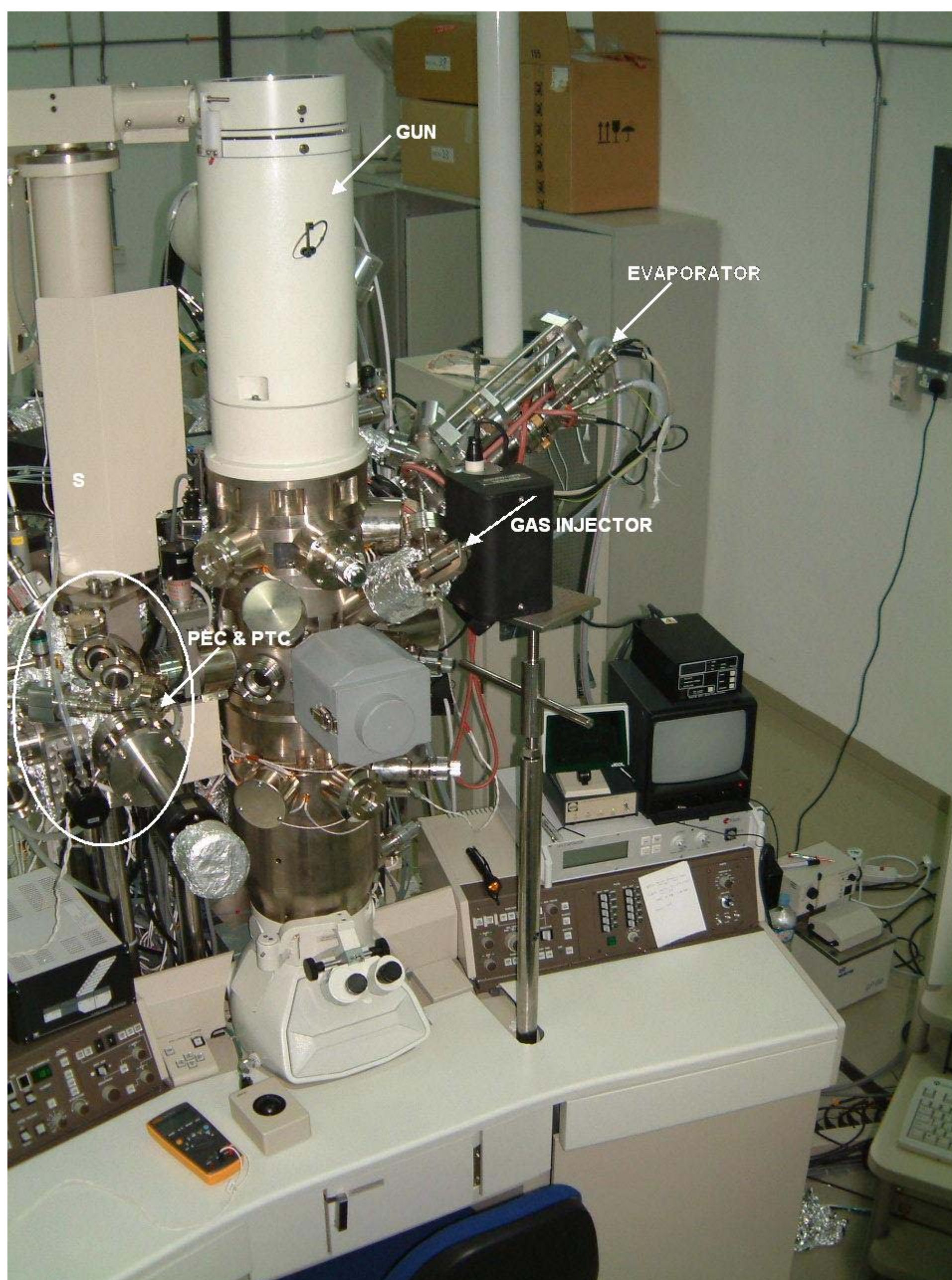

Figure 3.5 MERLION system

The **MERLION** system (a **M**odified **E**lectron-microscope for **R**ea**L**-time ***I****n-situ* **O**bservation on a **N**anoscale), is a JEOL 2000V UHV TEM. It essentially comprises a JEOL 2011 TEM modified for ultrahigh vacuum, *in-situ* heating and *in-situ* deposition of material from solid and gas sources. A photograph of the instrument is shown in Figure 3.5. The microscope is of high-resolution design, with a resolution of 1.9Å and equipped for analytical microscopy with an electron energy loss spectrometer (EELS) system energy filtered TEM capability. The base pressure is ~1.5×10^{-10}Torr.

The system is capable of operating at electron accelerating voltages of up to 200kV.

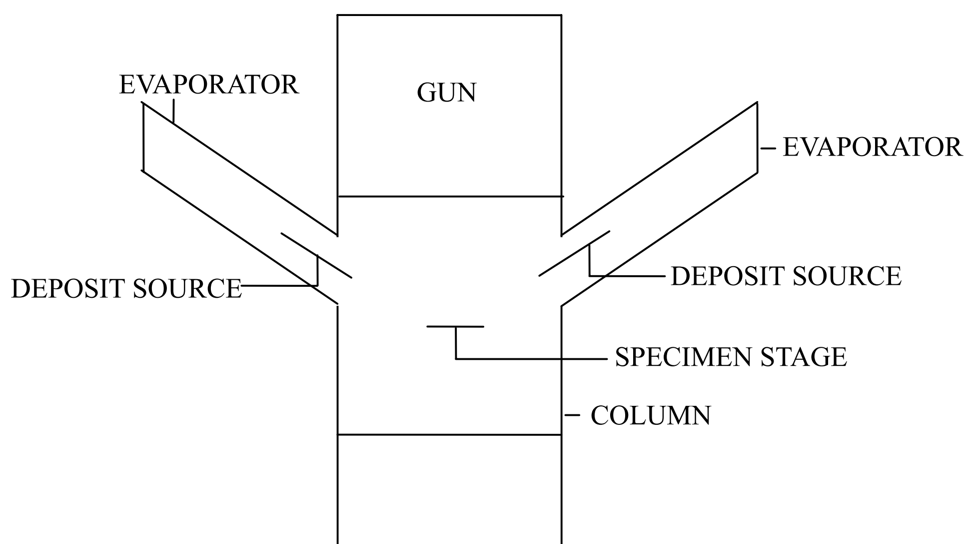

Figure 3.6 Schematic view of MERLION system

The specimen may be subjected to cleaning or other processing/growth in the pre-treating chamber (PTC). It may be heated, and/or treated by gas reaction in the

pre-treating chamber before microscopy if necessary. Special specimen holders if incorporated, allows the sample to be heated to in excess of 1200°C in the polepiece of the electron microscope whilst deposition is taking place and with the electron beam irradiating the region of the sample of interest.

3.2.1 Sample loading system

Figure 3.7 shows a schematic of the MERLION sample loading system and a main vacuum system. The samples are loading from PEC-PTC-Column, which is controlled by the valves between the columns. The valves can open only when the vacuum is adequate.

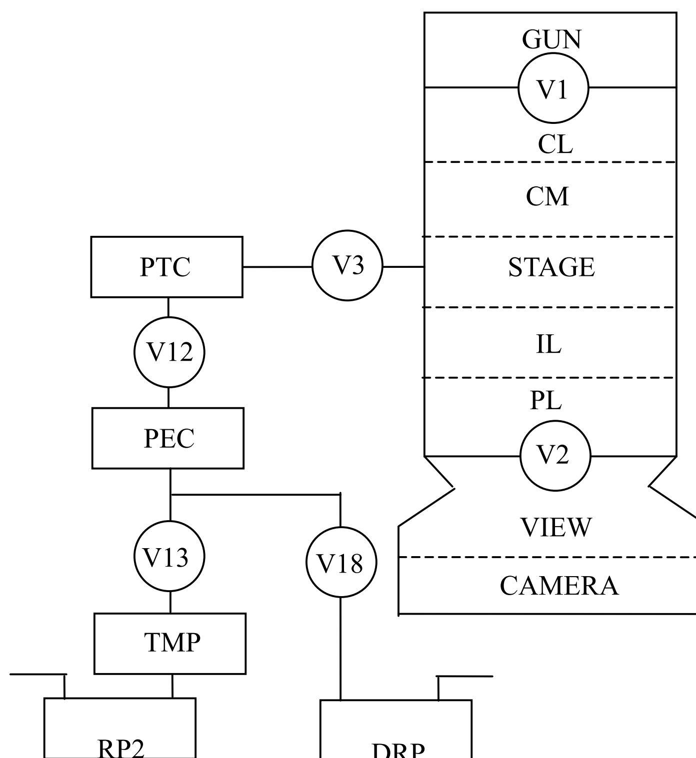

Figure 3.7 Schematic view of MERLION sample loading system.

3.2.2 Experiment system

The MERLION system enables deposition of metals onto different substrates,

and direct observation of nanostructure evolution. Deposition can be performed either by the electron beam evaporator, or by reactive gas injection, or both. Gas injection was not used for this project.

Electron beam evaporator[2]

In the UHV evaporator used on the MERLION, the evaporant is either evaporated from a bar, a rod or a crucible. This is achieved by electron bombardment heating. A key feature of the EFM is the integrated flux monitor, which allows the flux to be measured directly, hence permiting a much more precise rate adjustment and much faster rate control than an indirect tool such as thermocouple. It is designed for high precision sub-mono-layer up to multi-layer deposition of a wide variety of evaporants including highly refractory materials. It is used in combination with a 300W power supply.

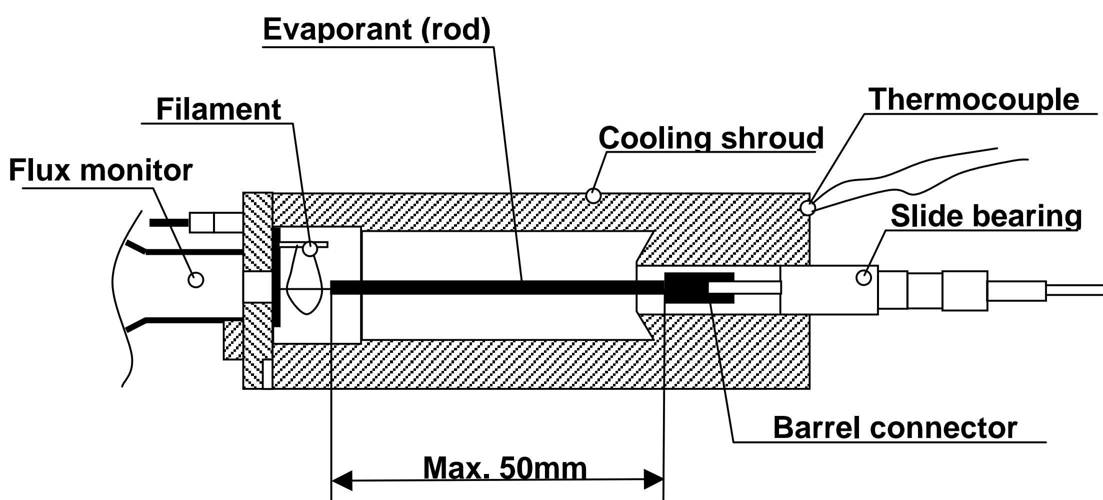

Figure 3.8 Evaporator fitting a rod

3.3 Sample preparation

For this experiment, MgO (Magnesium Oxide) substrate, cut with the substrate surface parallel to (100), were thinned to electron transparency by ion-beam milling prior to cleaning and loading in the microscope. The procedure is the same as normal TEM plan view sample preparation, with the addition of a high temperature cleaning stage. Figure 3.9 gives a schematic overview.

3.3.1 MgO(100) preparation

The MgO substrate (10×10mm) was cut into 2.5×2.5mm square pieces, followed by hand-grinding. SiC was used to grind the coarse face of the sample from 530μm to about 80μm~100μm. The sample was then dimpled to about 20μm on the same face, followed by ion milling to electron transparency at an angle of 7 degrees. Finally, e*x-situ* annealing at 820° C for 2 hours restored to crystalline order.

3.3.2 Si preparation

Si pieces (6mm×2mm) were cut from a silicon wafer and hand-grind from a thickness of 300μm to 230μm. The samples were then dimpled uniaxially to perforation forming a small hole of ~0.7mm square.

3.3.3 Sample Mounting

The annealed MgO substrate was mounted over the hole in the center of the silicon piece using CeramaBond 569-T adhesive, a ceramic bonding glue, with the small hole in MgO aligned over the comparatively large hole of the silicon piece.

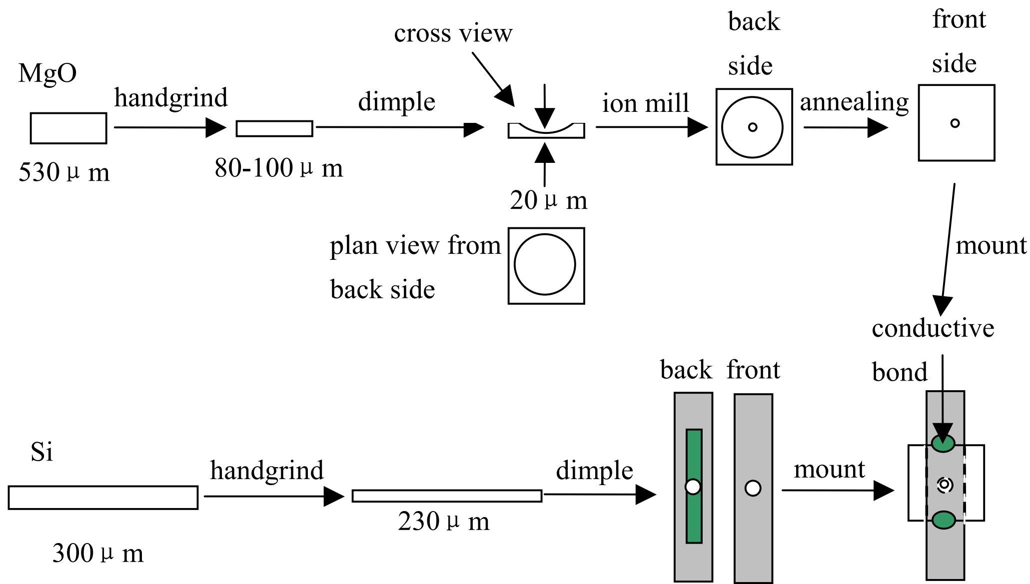

Figure 3.9 Schematic of the procedure of sample preparation.

3.3.4 Heating of MgO substrate and Calibration of Temperature

The MgO substrate was heated in our experiments during deposition of Ni atoms. The temperature was calibrated using a pyrometer; the chart of Figure 3.10 shows the measured temperature as a function of heating current; for temperatures below 400ºC a power law fit was used to extrapolate the curve from the high temperature regime.

All Si pieces were cut to the same size for consistency.

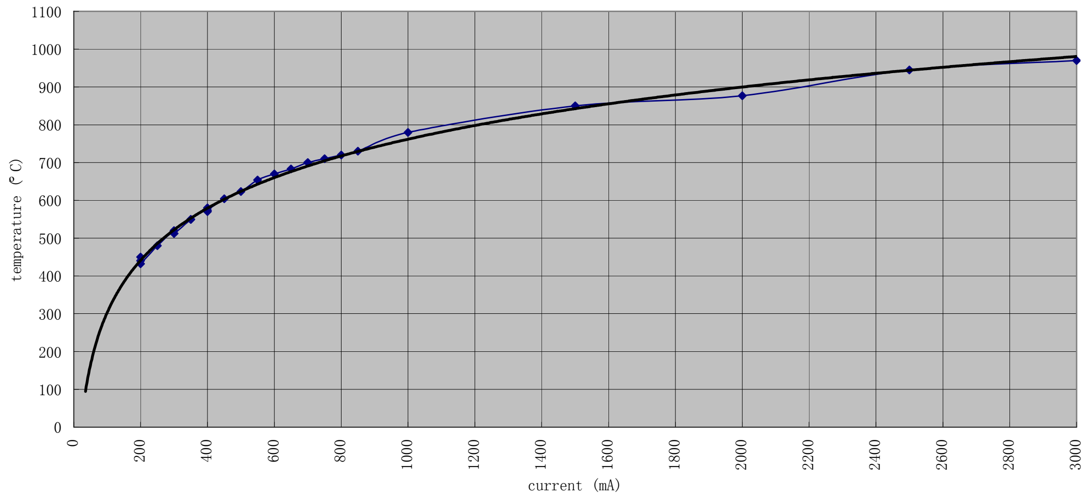

Figure 3.10 MgO current-temperature plot (the temperatures are measured by pyrometer), x-axis indicates the heating current, unit: mA; y axis indicates the substrate temperature, unit: ^{o}C.

3.4 MOKE Experimental Arrangements

A simple but widely used arrangement for performing MOKE measurements is shown schematically in Figure 3.11. It consists of a plane polarized laser beam (usually generated by a HeNe laser, λ=632.8nm) incident at an angle β upon the sample, which is mounted between the poles of an electromagnet. The reflected beam passes through an analyser and then to an optically screened Si photodiode.

A Hall sensor is attached to one of the pole pieces of the electromagnet to determine the magnetic field strength to which the sample is exposed.

The axis **G** of the crystal can be rotated in-plane with respect to the applied field ***H*** in order to study in-plane magnetic anisotropies (see Figure 3.11). The experiment may be computer controlled, enabling the magnetic field strength to be varied, whilst recording the photodiode signal as a function of the angular rotation of the crystal.

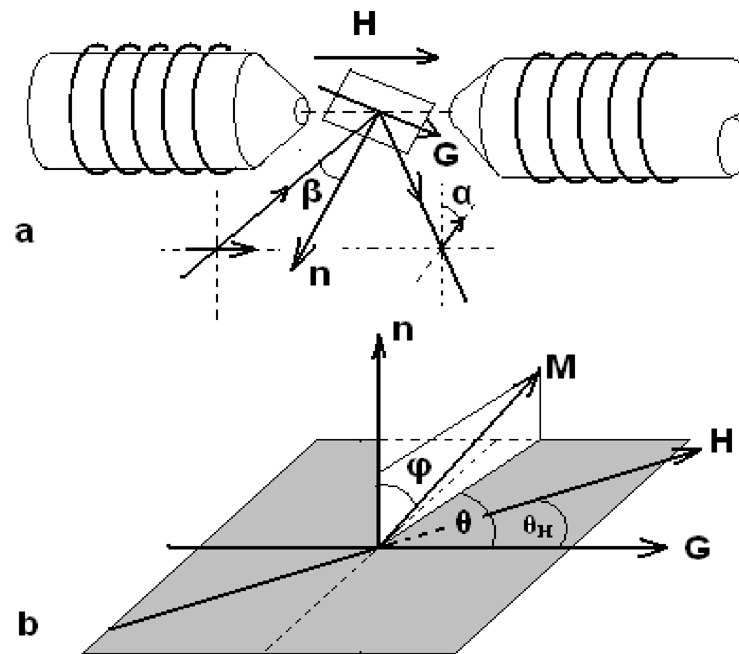

Figure 3.11 A schematic of a dc arrangement for observing the Kerr effect. The incident (laser) beam is polarized and incident at an angle β (typically 20˚) with respect to the sample normal ***n***. The sample can be rotated about the normal so that the angle between the applied field ***H*** and a specific crystal axis **G** can be vaired. The polarization is analysed by a polariser with transmission direction aligned at an angle α with respect to the scattering plane normal. The detector is not shown. (adapted from reference [3]).

References:

[1] D. B. Williams and C. B. Carter, *Transmission Electron Microscopy*, (Plenum Press, New York, 1996).

[2] Manual for EFM evaporator (Airpack Incorporated, 2000).

[3] J. A. C. Bland, *Polarized Electron/Polarized Photon Physics,* (Plenum Press, New York, 1995).

CHAPTER 4 Results & Discussion (I)

------------Crystal Structure

4.1 Initial Nucleation and Growth of Ni on MgO(100)

The early stages of the nucleation and growth of Ni on MgO(100) were studied over the temperature range of 25 - 550°C. We began by considering the results of growth at a temperature of 100°C. The flux of Ni atoms used for each experiment was maintained at a constant rate of ~0.33Å/min for all experiments unless otherwise stated. The deposition rate was calibrated using thickness measurements obtained by *ex-situ* Rutherford Backscattering Spectroscopy (RBS).

After stabilizing the sample at a temperature of 120°C, the shutter of the Ni evaporator was opened, and the electron diffraction patterns recorded at a rate of at least one every 20s. The first detectable evidence of the deposition on the MgO surface was observed after ~0.3nm nominal coverage of Ni. Discrete islands of Ni could be observed, and both images and selected area diffraction patterns were recorded. A representative diffraction pattern at this stage is shown in Figure 4.1 (a), with the beam close to [001]. The diffraction pattern shows the presence of cube on cube *fcc* Ni with the epitaxial orientation relationship:

Ni[100] // MgO[100]
Ni(001) // MgO(001)

The diffraction pattern corresponding to this orientation relationship, (the so-called cube on cube orientation) is shown in Figure 4.1 (b), together with the

diffraction pattern for MgO along the [001] zone axis in Figure 4.1 (a). The two patterns are shown superimposed in Figure 4.1 (c).

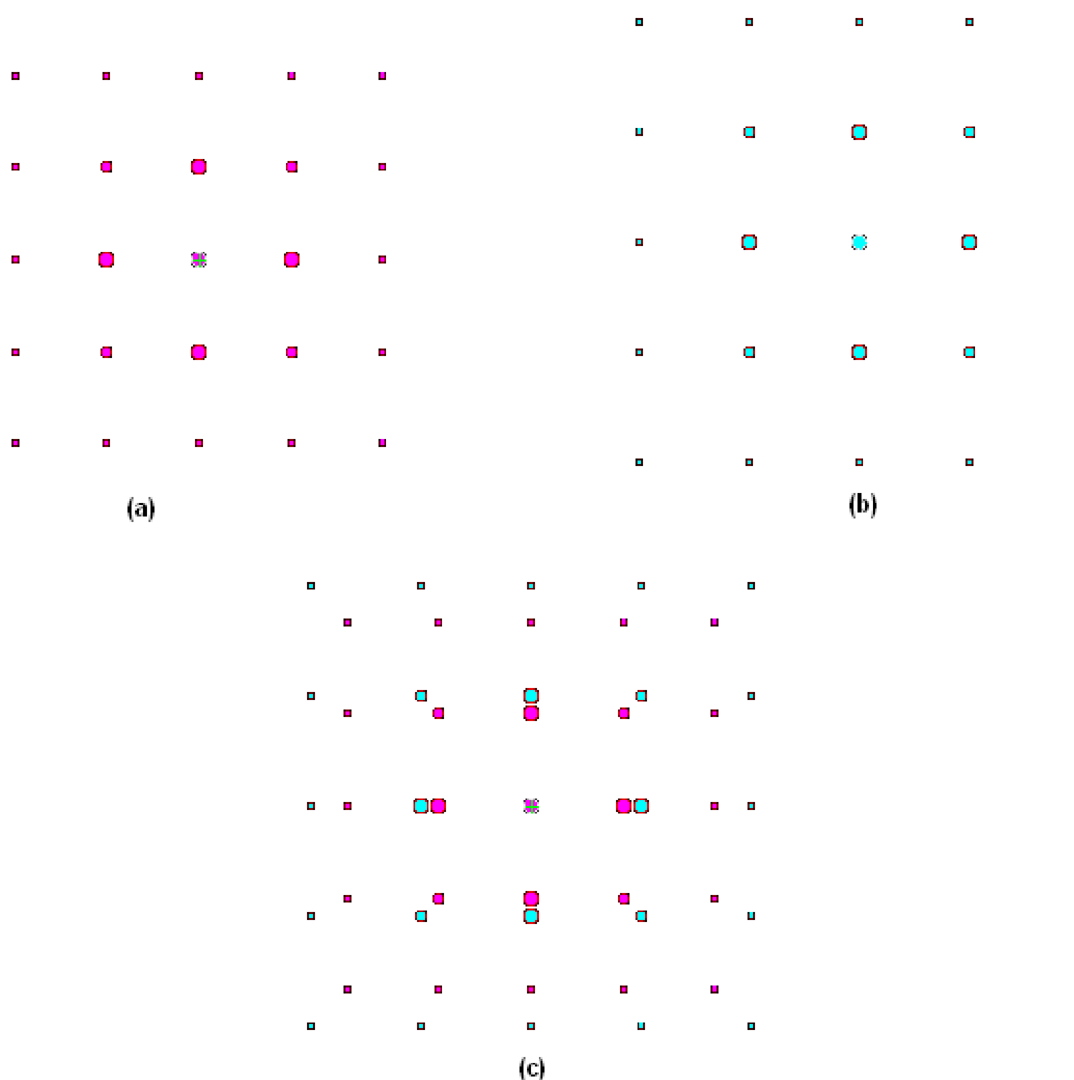

Figure 4.1 Computer simulations for the SAED pattern (a) simulation of the [001] zone axis SAED pattern of MgO; (b) simulation of the [001] zone axis SAED pattern of Ni; (c) superposition of (a) and (b).

In addition to the reflections due to [100] oriented Ni, a second set of reflections located between the 2h+1 2n 0 and 2n 2k+1 0 MgO reflections are also present. These reflections do not correspond to any known phase of Ni, or of nickel oxide. Reaction between Ni and MgO resulting in a mixed Ni-O or Ni-Mg-O

compound is very unlikely at deposition temperatures as low as 120°C. We consider now therefore the possibility of a structural transformation of our Ni epilayer.

Among the 3-D transition metals, structural transformations are well known in the case of Co, which undergoes a transformation between *hcp* and *fcc* phases at a temperature of 425°C. Ni however exhibits the *fcc* structure at all known temperatures. Stabilization of a *bcc* Ni structure has been achieved through epitaxy, however, when a thin film of Ni was deposited on the Fe (100) surface [1]. In a similar manner, stabilization of both *fcc*[2] Co and *bcc* Co[3,4] at room temperature has also been achieved.

Diffraction patterns for alternative Ni structures were simulated using the JEMS Software Package. Both *bcc* and *hcp* Ni phases were simulated. Only in the case of a novel hexagonal close-packed phase of Ni which has not been observed previously, was a possible fit observed. We consider this in more detail in the next section.

4.1.1 *hcp* Ni Phase

The diffraction data obtained were found to be in excellent agreement with a hexagonal close packed (*hcp*) phase of Ni, oriented with the [0001] axis in the plane of the substrate and parallel to the cube edges. Figure 4.2 (a) shows the simulated diffraction pattern for a MgO crystal with the beam parallel to [001]. In Figure 4.2 (b) we present a simulated diffraction pattern corresponding to an *hcp* Ni layer with the epitaxial orientation relationship:

$$Ni[0001] \,//\, MgO[100]$$

$$Ni(11\bar{2}0) \,//\, MgO(001)$$

A similar diffraction pattern is presented in Figure 4.2 (c), with Ni [0001] // MgO[010]; superimposition of the two patterns (Figure 4.2 (d)) produces a diffraction pattern which is in excellent agreement with the observed diffraction data, accounting for the presence of the effects of multiple diffraction.

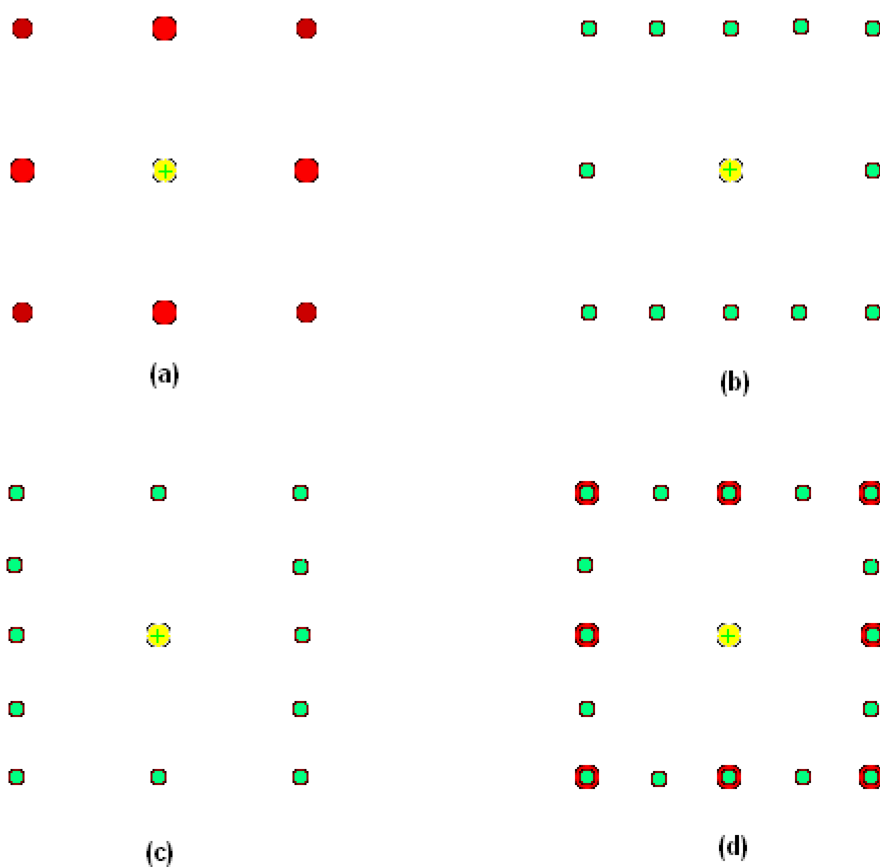

Figure 4.2 Computer simulations for the SAED pattern: (a) simulation of the [001] zone axis SAED pattern of MgO; (b) simulation of the $[11\bar{2}0]$ zone axis SAED pattern of *hcp*-Ni; (c) simulation of the $[11\bar{2}0]$ zone axis SAED pattern of an orthogonal growth variant, e.g. a 90° rotation counterpart to (b); (d) superposition of (a)(b)(c).

We believe that this novel *hcp* phase is stabilized by the formation of an initially pseudomorphic layer of Ni. The film must therefore adopt a structure similar to that of the surface structure of the substrate, in this case the MgO (100) surface. Strong Ni-O bonds are the most likely bonds to be formed as the first monolayer of Ni is deposited, to minimize the Coulomb interactions. Since Ni prefers a close packed structure, subsequent Ni adatoms will tend to locate at positions above four nearest-neighbour Ni atoms, thus forming a close-packed layer of Ni atoms in the plane perpendicular to an MgO<100> direction. This sequence gives rise to a close packed Ni structure identical to the *hcp* alignment such that Ni[0001]//MgO[100] and Ni[$10\bar{1}0$] // MgO[010]. The Ni atoms will be displaced slightly from the O^{2-} locations as shown in Figure 4.3.

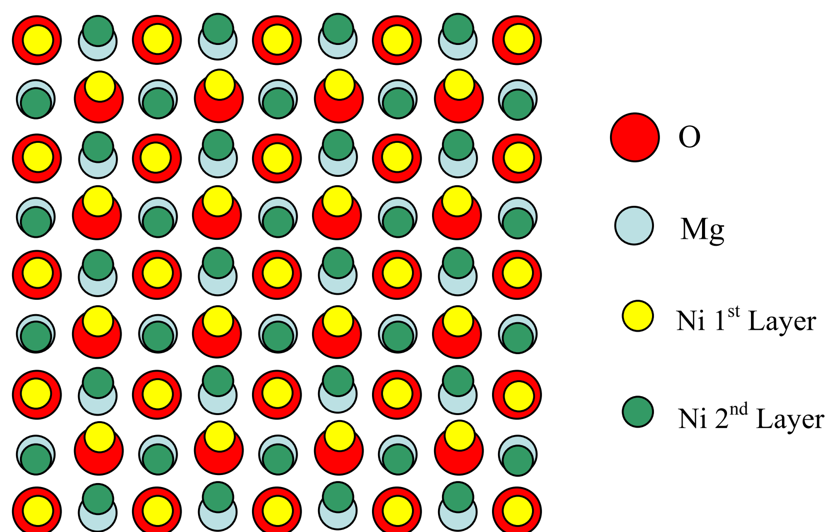

Fig 4-3 Diagram showing the arrangement of the first two monolayers of Ni grown on (001) MgO

The c/a ratio of the *hcp* phase is found to differ from the ideal value of 1.633, having a value of 1.729, 6% higher than the ideal value. The *hcp* layer is thus pseudomorpically strained in order to optimize the interfacial electrostatic structure and the tendency for Ni to assume a close-packed crystal structure.

As we have previously noted, the lattice mismatch between Ni and MgO(100) for the cube-on-cube orientation is ~16%. For the pseudomorphically strained *hcp* Ni phase in the orientation observed here, the interfacial mismatch along the [100] and [010] directions are 1.8% and 3.9%, respectively.

Whilst the *hcp* structure in the orientation observed shows a smaller lattice mismatch with MgO (100), we should also consider any increase in lattice energy of the Ni structure in the *hcp* form compared with the expected *fcc* form. First-principles calculations using the plane-wave pseudo-potential method suggest the difference in lattice energy between *hcp* and *fcc* Ni to be $\Delta E_{lattice} = E_{hcp} - E_{fcc} = +0.025$ eV/atom. The *hcp* structure thus has a slightly higher lattice energy. It is clear, however, that the decrease in lattice mismatch of the *hcp* phases with MgO (100) is able to offset the increased lattice energy of the *hcp* structure. The resulting difference in the strain energy of the systems is estimated to be $\Delta E_{strain} \approx -0.25$eV/atom. This is an order of magnitude larger and of opposite sign to the difference in lattice energy and thus dictates the formation of nanoscopic *hcp* Ni islands during the very early stages of growth.

The presence of a small fraction of *fcc* Ni islands of cube-on-cube orientation in the early stages of growth is possibly due to thermal fluctuations since the difference in lattice energy between *hcp* and *fcc* Ni is believed to be small. *Fcc* Ni can also be generated by the introduction of stacking faults in the *hcp* structure.

At higher growth temperatures, some (110) oriented *fcc* Ni islands were also observed in the early stage of growth. This orientation will be discussed in the next section.

Our primary interest in Ni thin films is for their practical application as a magnetic storage medium. The magnetic properties of *hcp* Ni (and *hcp* Co and Cr, in addition) have in fact been modeled using the Stoner theory of ferromagnetis [5,6,7] by Papaconstantopoulos et al [8]. To investigate the properties, these elements were expected to be stabilized in the *hcp* phase. The properties of ferromagnetic *hcp* Ni were expected to be similar to that of ferromagnetic *hcp* Co, therefore *hcp* Ni is predicted to exhibit a magnetic moment of 0.76μ_B per atom, and spin splitting of 0.1Ry.

The possibility of synthesizing new phases of 3-D transition metal elements with enhanced magnetic properties is an exciting prospect.

4.1.2 Transformation from *hcp* Ni to *fcc* Ni

As deposition of Ni atoms continued, a new set of diffraction spots began to appear. A corresponding decrease in the intensity of the *hcp* reflections was also observed. The new diffraction pattern was found to correspond to a (110) orientation

of *fcc* Ni, i.e. with Ni (110) parallel to the MgO(100) surface. Two distinct orientation relationships were determined from the diffraction pattern. In the first orientation, Ni [001] is parallel to the MgO [110] direction. There are two possible orientations for this case, obtained by 90° rotation. In the second orientation, the Ni [111] direction is parallel to the MgO [100] direction. There are four possible orientations in this case, plus a further four due to twinning.

These orientations are indexed in the diffraction pattern of Figure 4.4. The bold white circles indicate reflections from grains with an in-plane orientation of *fcc*-Ni $[\bar{1}1\bar{1}]$//MgO[100]. The reflections marked with regular white circles are in a mirror relationship with respect to the bold circles, and the mirror plane is along the MgO [010] direction. This corresponds to a twin relationship, the mirror plane being the close-packing {111} plane of *fcc*-Ni. Due to a four-fold degeneracy of the (001) face of MgO, a 90 degree rotation of both of the bold and regular reflections will generate the rest of the *fcc*-Ni (110) reflections in Figure 4.4.

The (110) orientation of Ni results in a lattice mismatch slightly higher than that of *hcp* Ni in the orientation observed in the early stages of growth, being 2.4% and 3.4% along orthogonal [100] directions of the MgO lattice for (110) oriented *fcc* material.

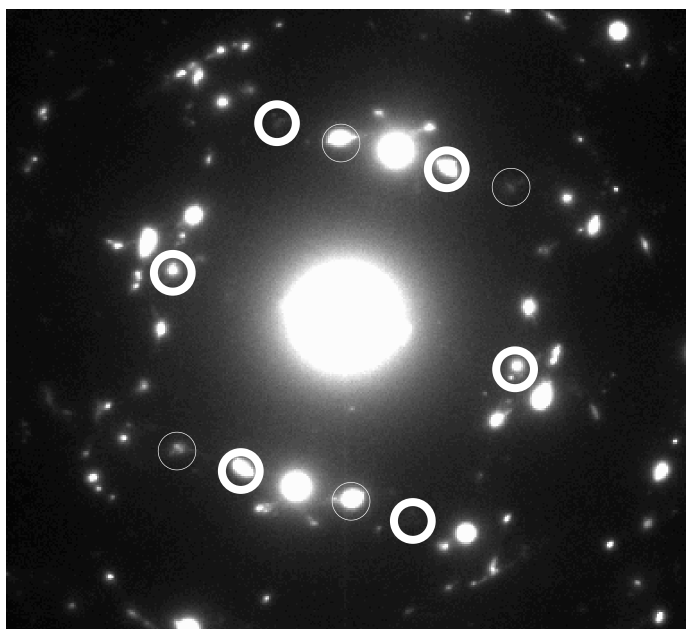

Figure 4.4 SADP indicating a Ni (110) epitaxial relationship, with the bold white circle indicating the orientation of Ni [$\bar{1}1\bar{1}$]//MgO [100], the regular white circle indicating a mirror relationship to the bold white circle along the MgO [010] direction.

The transformation between the *hcp* Ni and *fcc* Ni structures was observed to occur at a nominal substrate coverage of between ~3.6 and 4.8nm.

Hcp to *fcc* transformations are observed in other materials systems, and the classical martensitic transformation mechanism is very likely responsible for the structural transformation observed here. The martensitic transformation has been well studied in metals[9,10] since the change in stacking sequence from ABAB… (for the *hcp* structure) to ABCABC (for the *fcc* structure) can occur by the introduction of stacking faults through glide on close packed planes, which is a relatively low energy process.

The process of transformation is illustrated schematically in Figure 4.5. A translation of the positions of the atoms in column b1 produces an aba**cab** stacking sequence, resulting in a local *fcc* stacking sequence (i.e. ..**cab**…). In the real crystal

lattice this would occur by glide of the b plane atoms to the position of the c plane in *fcc* Ni, such that atoms B_1 and $B_1^{'}$ glide to positions C_1 and $C_1^{'}$. Similarly, the atoms in column a_3 can glide to the c plane position, such that atoms A_3 and $A_3^{'}$ now occupy positions C_2 and $C_2^{'}$. The net formed by connecting C_1, C_2, $C_2^{'}$ and $C_1^{'}$ matches that of the Ni (110) surface. In the case of Figure 4.5, columns a_3 and b_2 now lie either side of a stacking fault in the Ni lattice, bounding regions of *hcp* Ni and *fcc* Ni, to the left and right respectively.

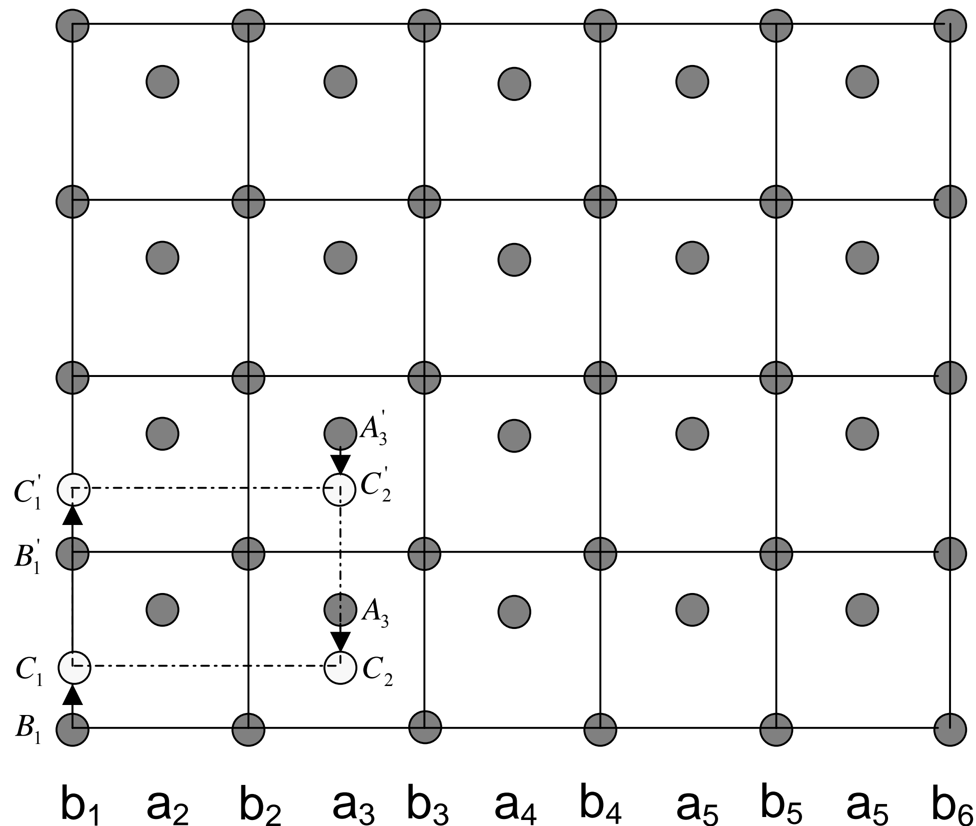

Figure 4.5 A schematic illustration of an *hcp*→*fcc* martensitic phase transformation through the staking faults mechanism.

Clearly a mixture of phases within a single particle is possible, and during the course of the experiments attention was given to identifying the spatial origin of the

hcp and *fcc* contributions to the diffraction patterns. Dark field images recorded from the same area of the sample using *hcp* and then *fcc* Ni reflections revealed diffraction intensity from the same spatial regions of the samples, and both vertical and lateral variations in composition could be identified.

Our observations are reminiscent of the phenomenon of contact epitaxy observed in Ag nanoparticles deposited on the Cu (100) surface[11]. The particles, formed prior to deposition by inert-gas condensation in an inert carrier gas, were deposited on the clean Cu surface at room temperature. Dark-field images recorded immediately following deposition showed the particles to comprise several monolayers of (111) oriented, epitaxial Ag at the interface with the Cu surface, with the remainder of the particle being of an apparently random orientation. The formation of an epitaxial layer evidently occurred upon contact between the particle and the substrate. The surface energy of a particle of diameter ~5nm is substantially different from that of the bulk material, and the driving force to minimize this energy through interfacial bonding can be substantial.

4.2 Phase Composition as a Function of Temperature

The variation in composition as a function of thickness and growth temperature was studied in order to further understand the Ni/MgO system. The aim of these experiments was to construct a phase diagram of the structure and orientation of the Ni

deposit as a function of thickness and growth temperature. The experiments were performed at temperatures from room temperature to 550°C.

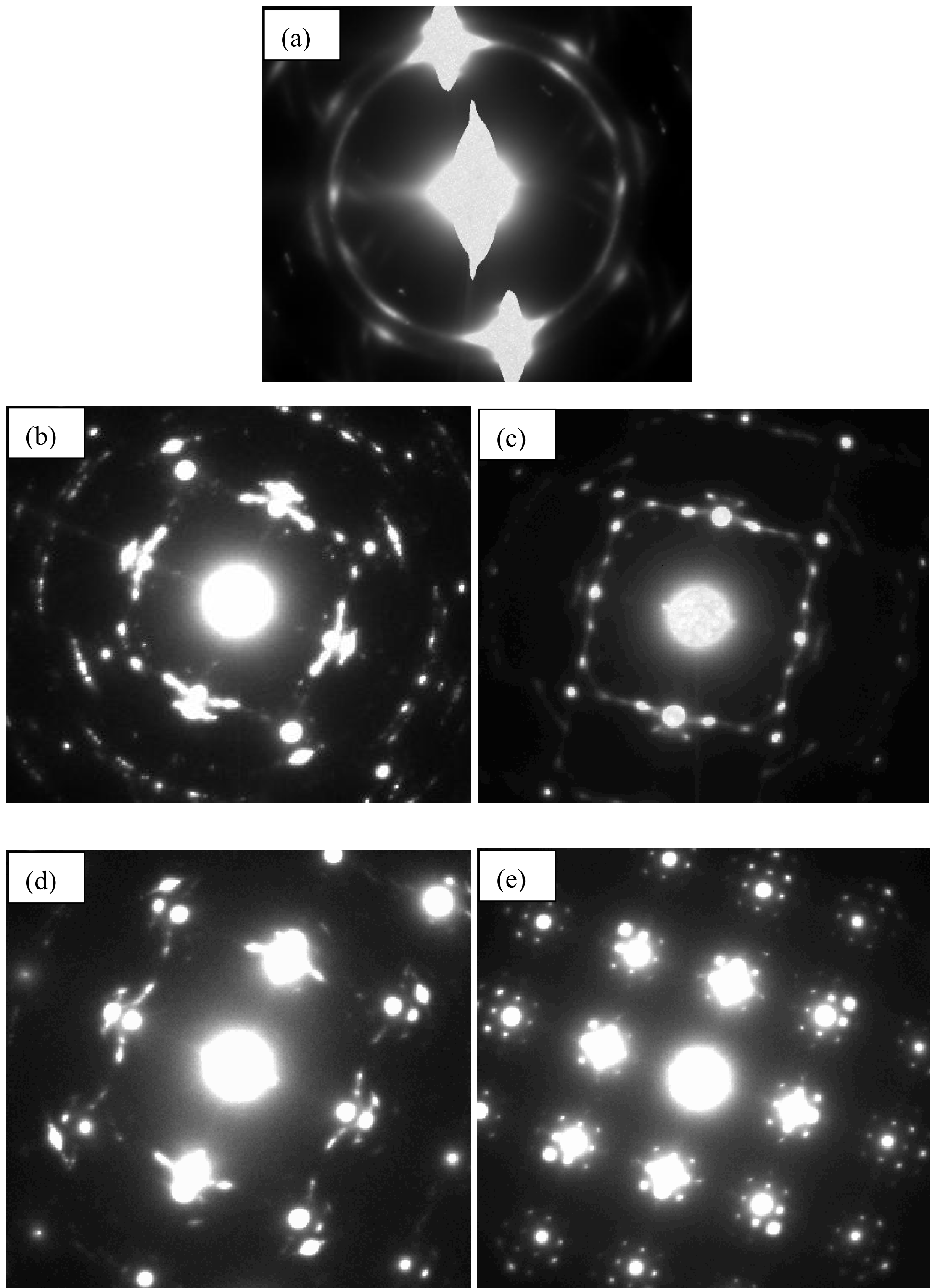

Figure 4.6 A sequence of selected area diffraction patterns recorded at a film thickness of 5nm at temperatures of (a)→(e): 25°C, 50° C, 100° C, 300° C and 550° C, respectively.

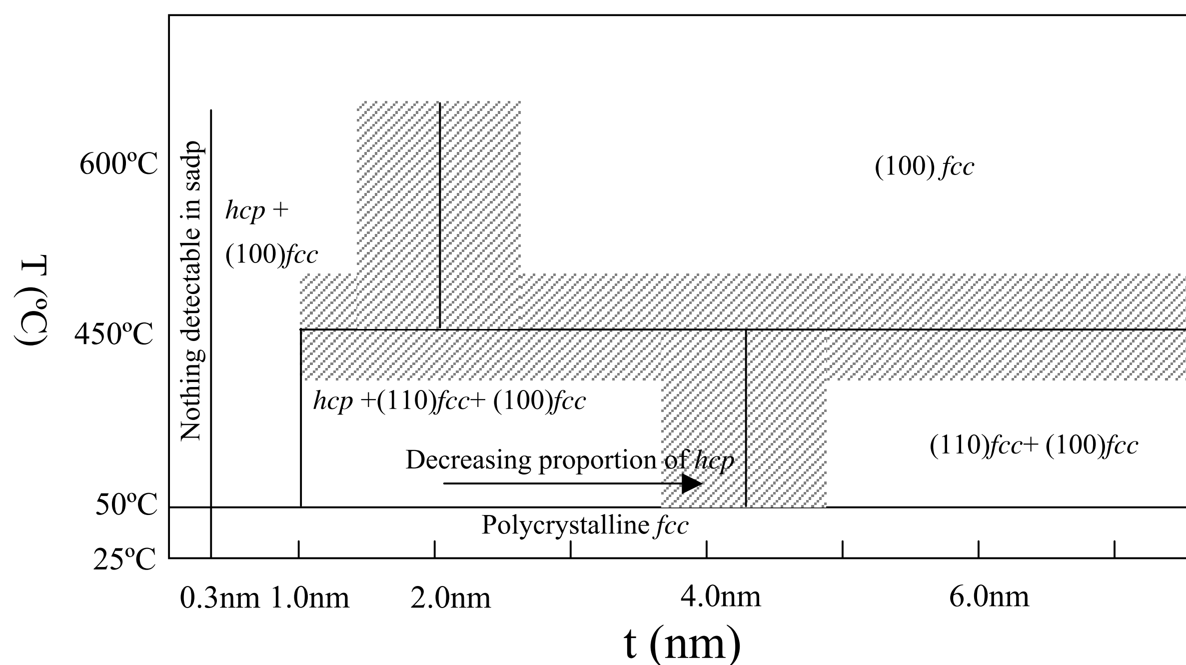

Figure 4.7 Phase diagram as a function of growth temperature and thickness, for Ni on MgO(100).

In Figure 4.6 we show a sequence of selected area diffraction patterns recorded at a nominal film thickness of 5nm at temperatures of 25°C, 50° C, 100° C, 300° C and 550° C. At a temperature of 25° C, the presence of polycrystalline Ni is apparent, at 50°C the film is predominantly of single crystal orientation, and above this temperature the films are of entirely single crystal orientation. The dominant epitaxial orientation below 550°C is the (110) orientation, whilst at 550°C the film is of (100) orientation. No evidence of (110) oriented Ni was observed at any stage during growth at 550°C. The phase diagram constructed from the data obtained during the studies is presented in Figure 4.7.

It can be seen from the diagram that, at temperatures above ~500°C the *hcp* Ni formed in the early stages of growth transformed directly to (100) oriented Ni with no intermediate (110) orientation observed.

Our results may be understood by a consideration of the competition between the minimization of surface energy, versus interfacial energy, in the growing deposit. The lattice mismatch between the (100) surfaces of Ni and MgO is ~16%; in contrast, for (110) orientated Ni, the mismatch is substantially lower, being 2.4% and 3.4% along orthogonal [100] directions of the MgO lattice. This was discussed by Raatz and Woltersdorf[12], who studied the growth of Ni on MgO(100) over the temperature range 400-600°C at film thicknesses of between 20 and 65nm. At the low end of this thickness range, their films were found to be entirely of (100) orientation, with a transformation to (110) orientation observed at higher thicknesses. Their studies did not, however, explore films below 20nm thickness, as have been investigated in the present studies.

In our experiments, the Ni lattice have been found to assume an *hcp* structure with the $(11\bar{2}0)$ plane pseudomorphically strained to match the MgO (100) surface at the lowest coverages; in addition, (100) oriented *fcc* material is observed. As the island size increases, at temperatures of 450°C and below, the *hcp* phase transforms to (110) oriented Ni, which has a higher surface energy than (100) oriented Ni[13], but a much lower lattice mismatch.

At temperatures of 500ºC and above, the formation of (110) Ni in the early stages of growth is suppressed, and the *hcp* phase transforms to (100) oriented Ni. At these elevated temperatures the minimization of surface energy is clearly preferred over that of interfacial energy. The lattice mismatch between Ni and MgO in cube on cube orientation is ~16.18% at room temperature, increasing with temperature to ~17.28% at 550ºC.

Honjo and Yagi [14] performed *in-situ* growth studies, using a modified UHVTEM, for a variety of metals on (100) MgO including Ni, Pd, Cu, Pt, Al, Fe, Ag and Au. They concluded that the various epitaxial orientations observed were systematically dependent on the lattice mismatch between the substrate and deposit. Their films, which were also discontinuous and in the form of discrete islands, showed a small amount of (110) oriented Ni, but were predominantly of (100) orientation. In contrast to our experiments, no *hcp* phases were observed, and no transitions between orientations reported.

This may be due to the fact that, in our experiments, the growth rate (~0.33Å/min) is relatively low, enabling us to study the temporal development of the very earliest stages of growth in some detail before the *hcp* phase transforms to the *fcc* phase at higher coverages. In the case of the experiments of Honjo and Yagi[14], this stage of the growth sequence may have occurred within a time period of less than one second, making detection of the *hcp* phase from the diffraction data more challenging.

4.3 High temperature annealing of Ni deposits

In order to explore in more depth the relationship between the phases represented in the phase diagram, high temperature annealing experiments were performed on films grown at relatively low temperatures. In this way, the thermal stability of the $(11\bar{2}0)$ *hcp* Ni phase with respect to the (110) or (100) oriented *fcc* phase could be investigated.

For the first experiment, a film was grown to a nominal thickness of 0.8nm at a temperature of 100ºC. A selected area diffraction pattern recorded immediately upon completion of growth at 100ºC is shown in Figure 4.8 (a). The film was of primarily $(11\bar{2}0)$ oriented *hcp* Ni, with a small amount of (100) oriented *fcc* Ni. The film was then annealed to temperatures in excess of 800ºC in stages, with diffraction patterns and the corresponding images recorded at each stage.

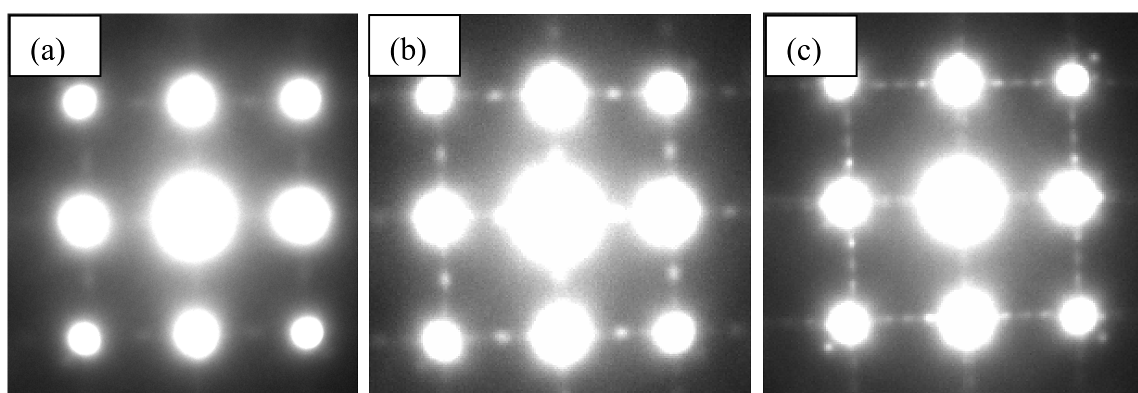

Figure 4.8 SADPs as a function of temperature following deposition of a Ni layer of nominal thickness 0.8nm at 100ºC. (a) sadp immediately after completion of Ni growth; (b) sadp at the annealing temperature of 650ºC; (c) sadp at the annealing temperature of 720ºC.

At a temperature of ~650ºC, the *hcp* and (100) *fcc* reflections were still apparent, as can be seen in the diffraction pattern of Figure 4.8 (b). At ~720ºC (Figure 4.8 (c)), the $(11\bar{2}0)$ *hcp* reflections have reduced significantly in intensity, the presence of (110) oriented *fcc* Ni, in addition to (100) oriented *fcc* Ni.

The sample was then heated to ~820ºC before being cooled to room temperature. No further transformations or reorientations were observed either during the final heating stages, or during cooling to room temperature.

Annealing of films composed of entirely *fcc* Ni, of (110) orientation was then performed, to explore the possibility of reorientation of the *fcc* phase during temperature excursions. Films were grown at 100ºC and 400ºC, to thicknesses of 40nm and 12nm respectively.

In the case of the film grown to a thickness of 40nm at 100°C, the entire substrate surface had become wetted by the deposit, and annealing at 400ºC led to a transformation from entirely (110) oriented material, to entirely (100) oriented material, after approximately 1 minute at 400ºC. No pinhole formation or agglomeration was observed during the transformation.

In the case of the 12nm film, grown at a temperature of 400°C, the film was comprised of discrete islands of Ni, of both (100) and (110) orientation. Annealing from 400ºC to 900ºC led to no change in orientation of the film, although some coarsening of the islands was observed consistent with an Ostwald ripening mechanism.

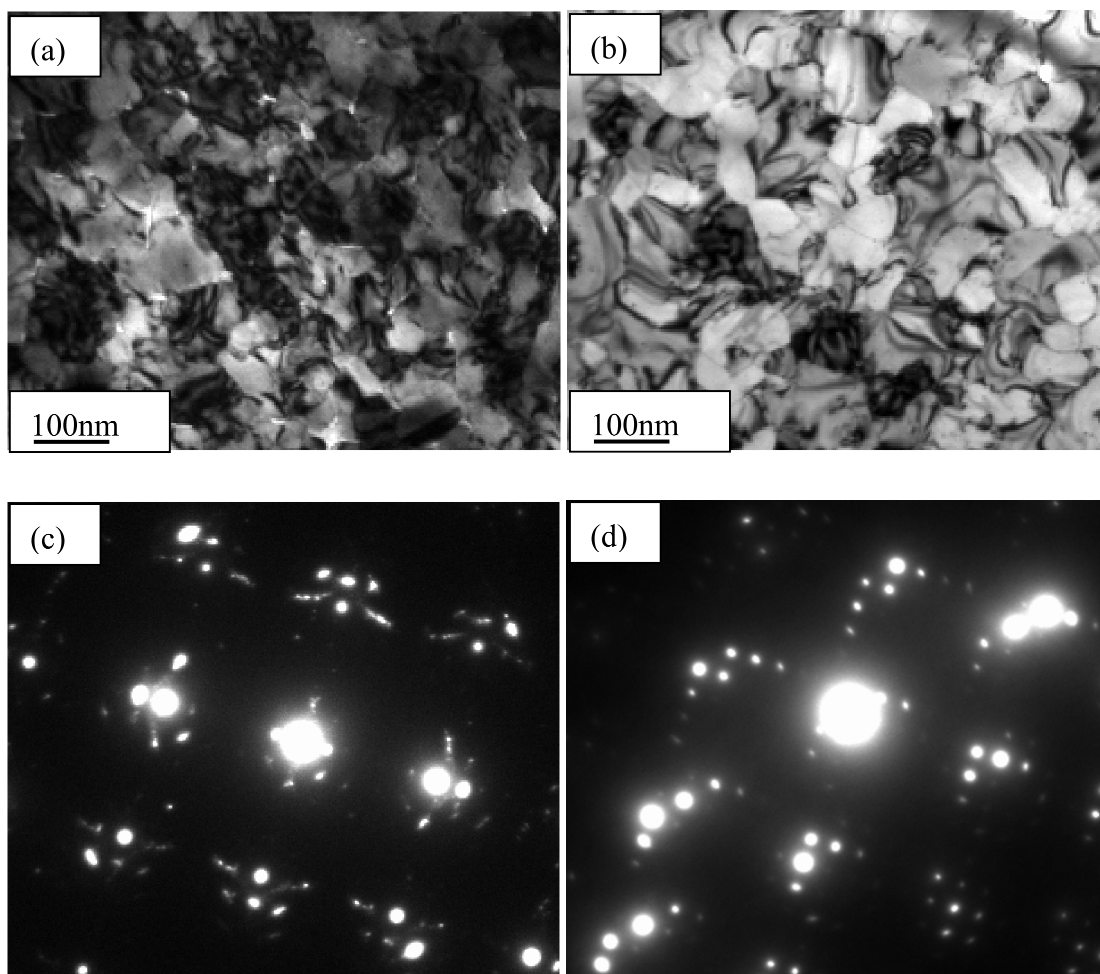

Figure 4.9 Bright field image and diffraction pattern comparison before and after anneal: (a) bf image before anneal; (b) bf image after anneal; (c) diffraction pattern before anneal; (d) diffraction pattern after anneal.

The results of the annealing of the film grown at 100ºC are presented in Figure 4.9. Bright-filed images recorded before and after annealing at 400ºC are presented in Figure 4.9 (a) and (b), respectively, with the corresponding selected area diffraction patterns being presented in Figure 4.9 (c) and (d), respectively.

Our observations suggest that, in the smallest islands, the *hcp* phase is well stabilized with respect to temperature, with full transformation to *fcc* phase only occurring above 700ºC in the absence of fresh deposit. This transformation may be due, at least in part, to a small amount of coarsening of the islands during annealing,

potentially equivalent to an increase in deposit thickness in terms of the phase diagram of Figure 4.7. For the continuous film, 40nm in thickness, grown at 100°C, the (110) *fcc* orientation is the lowest energy configuration until the film is annealed to 400°C. At this temperature, the minimization of interfacial energy clearly predominates over the minimization of misfit strain energy and the transformation to (100) orientation is observed. This is entirely consistent with the observations of Raatz and Woltersdorf. In their experiments, an initially (100) oriented *fcc* Ni film underwent reorientation to a (110) orientation at a critical thickness where the elastic strain energy stored in the epilayer is sufficient to initiate the reorientation process. The (110) oriented domains, composed of twin lamellae, reduce the lattice mismatch at the interface and thus reduce the overall interfacial energy of the system. The reduction in the interfacial energy clearly offsets the increase in energy due to the formation of the twinned (110) domains.

As the thickness of the layer increases, however, the strain energy stored in the twin domains will increase until, at a critical thickness, the twin energy exceeds the reduction in interfacial energy that may be gained by assuming the (100) orientation. Whilst this reorientation was not favourable at 100°C, in the case of the 40nm film grown at this temperature, upon annealing to 400°C sufficient thermal energy to initiate this reorientation process was available. The transformation presented in Figure 4.8 was thus able to occur.

In the case of the discontinuous film (12nm thick) grown at 400°C, reorientation to (100) domains would be unlikely to occur even at elevated temperatures since the reduction in interfacial energy due to the (110) oriented domains is likely to exceed the strain energy stored within the twin domains at such low deposit thicknesses even at elevated temperatures. Thus no reorientation is observed, even at the annealing temperature of 900°C achieved in the present work. For discrete island nuclei, additional strain relaxation by lateral expansion of the islands (a morphological effect) could also contribute to the minimization of the free energy of the island.

References:

[1] F. J. Lamelas, C. H. Lee, H. He, W. Vavra and R. Clarke, Phys. Rev. B, 40, 5837 (1989).
[2] B. I. Min, T. Oguchi and A. J. Freeman, Phys. Rev. B, 33, 7852 (1986).
[3] G. A. Prinz, Phys. Rev. Lett., 54, 1051 (1985).
[4] H. L. Skriver, Phys. Rev. B, 31, 1909 (1985).
[5] J. F. Janak, Phys. Rev. B, 16, 255 (1977).
[6] E. C. Stoner, Proc. R. Soc. London, Ser. A, 169, 339 (1939).
[7] J. L. Fry, Y. Z. Zhao, P. C. Pattnaik, V. L. Moruzzi and D. A. Papaconstantopoulos, J. Appl. Phys., 63, 4060 (1988).
[8] D. A. Papaconstantopoulos, J. L. Fry and N. E. Brener, Phys. Rev. B, 39, 2526 (1989).
[9] G. B. Olson and M. Cohen, Matell. Trans. A, 7, 1897 (1976).
[10] H. Fujita and S. Ueda, Acta Metallogr., 20, 759 (1972).
[11] M. Yeadon, J. C. Yang, M. Ghaly, R. S. Averback and J. M. Gibson, Appl. Phys. Lett., 73, 3208 (1998).
[12] G. Raatz and J. Woltersdorf, Phys. Stat. Sol. (a), 113, 131 (1989).
[13] P. Deurinck and C. Creemers, Surf. Sci., 441, 493 (1999).
[14] G. Honjo and K. Yagi, in: *Current Topics in Materials Science,* (North-Holland, 1980).

CHAPTER 5 Results & Discussion (II)

-------------Surface Diffusion, Island Coalescence and Magnetic Properties

5.1 Activation Energy for Surface Diffusion

It is well established from classical nucleation theory that the activation energy for surface diffusion of depositing species over a substrate surface may be calculated from a measurement of the initial saturation nucleation density of deposit islands[1].

The saturation island nucleation densities were determined from our data from the earliest stages of film growth; the data are presented in Table 1.

Table 5.1 Saturation island nucleation densities at different growth temperatures.

Temperatures	100°C	300°C	380°C	450°C	550°C
Saturation nucleation densities (per cm^2)	$7.94x10^{12}$	$2.92x10^{12}$	$3.60x10^{12}$	$1.20x10^{12}$	$1.00x10^{12}$

The logarithm of the saturation nucleation density was then plotted as a function of $1000/T_g$, where T_g is the growth temperature for that sample. The results are presented in Figure 5.1. From the slope of the plot, a value for the activation energy for surface diffusion of Ni on MgO(100) was determined to be ~0.6eV.

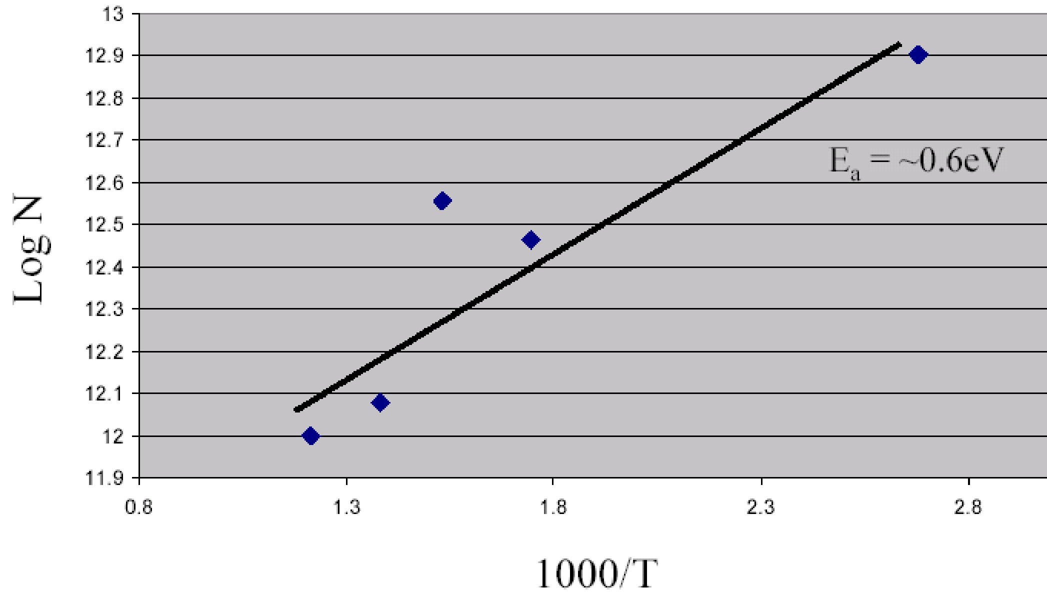

Figure 5.1 Arrhenius plot of Log (saturation nucleation density) as a function of $1000/T_g$, where T_g is the growth temperature.

In Figure 5.2 we present a sequence of bright-field images of the saturation nucleation stage of films grown at 50°C (Figure 5.2 (a)) and 100°C (Figure 5.2 (b)). The decrease in nucleation density with temperature may be clearly discerned from the images.

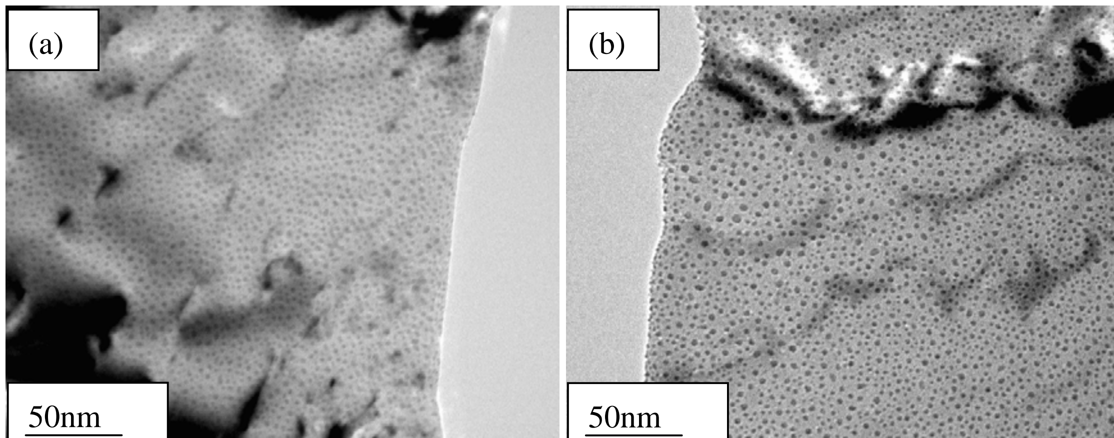

Figure 5.2 Bright-field images recorded during the early stages of film growth at the point of maximum nuclei density (the saturation nucleation density) for substrate temperatures of (a) 50°C and (b) 100°C.

To our knowledge there are no previously reported experimental values of the activation energy for Ni diffusion on MgO. A value for surface self diffusion of Ni has been determined, and is in fact similar to the value we obtain for Ni on (100) MgO[2,3]. First principle calculations of the interactions of both Ni atoms and clusters of Ni atoms with the MgO(100) surface were performed, however, and showed that Ni atoms prefer to bond to the surface oxygen atoms. This is consistent with the large free energy of formation of NiO[4]. Further investigations of the activation energy of Ni on different surfaces of MgO are planned in order to further understand our observations.

5.2 Island Coalescence

Observations of island coalescence were made during the course of the experiments as a function of growth temperature, between room temperature and 600°C. At temperatures of 100°C and below, the rate of coalescence was low, and, once a particular area of the substrate had become wetted by the deposit, dewetting of that area was not subsequently observed.

A sequence of images recorded during the earliest stages of island coalescence is shown in Figure 5.3, where the transformation from the pseudomorphically strained *hcp* and (100) oriented *fcc* phase to the mixed (110) and (100) oriented *fcc* phase is observed. The images were recorded after (a) 0.21nm, (b) 0.3nm, (c) 0.45nm and (d) 0.75nm nominal deposition.

During the later stages of film coalescence, multiple orientations of crystallites within a single island could be observed, and a representative image is presented in Figure 5.4. The presence of moiré fringes in the image enables ready identification of the boundaries between grains of different in-plane orientations.

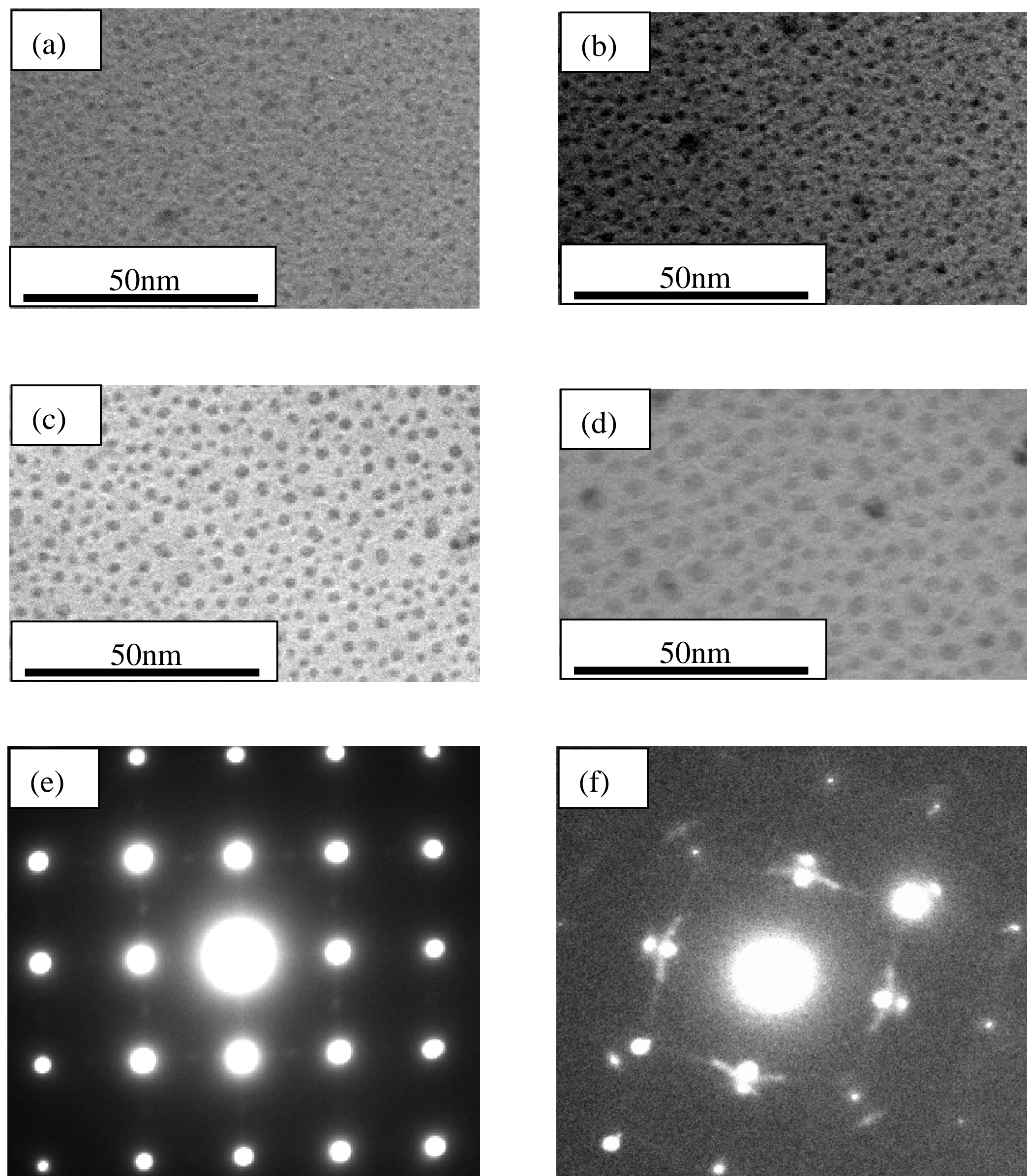

Figure 5.3 Images and diffraction patterns (inset), corresponding to the transition from *hcp* to *fcc* Ni during growth at 100°C at different nominal thicknesses. (a) 0.21nm; (b) 0.3nm; (c) 0.45nm; (d) 0.75nm; (e) corresponding SAD pattern of image (a); (f) corresponding SAD pattern of image (d).

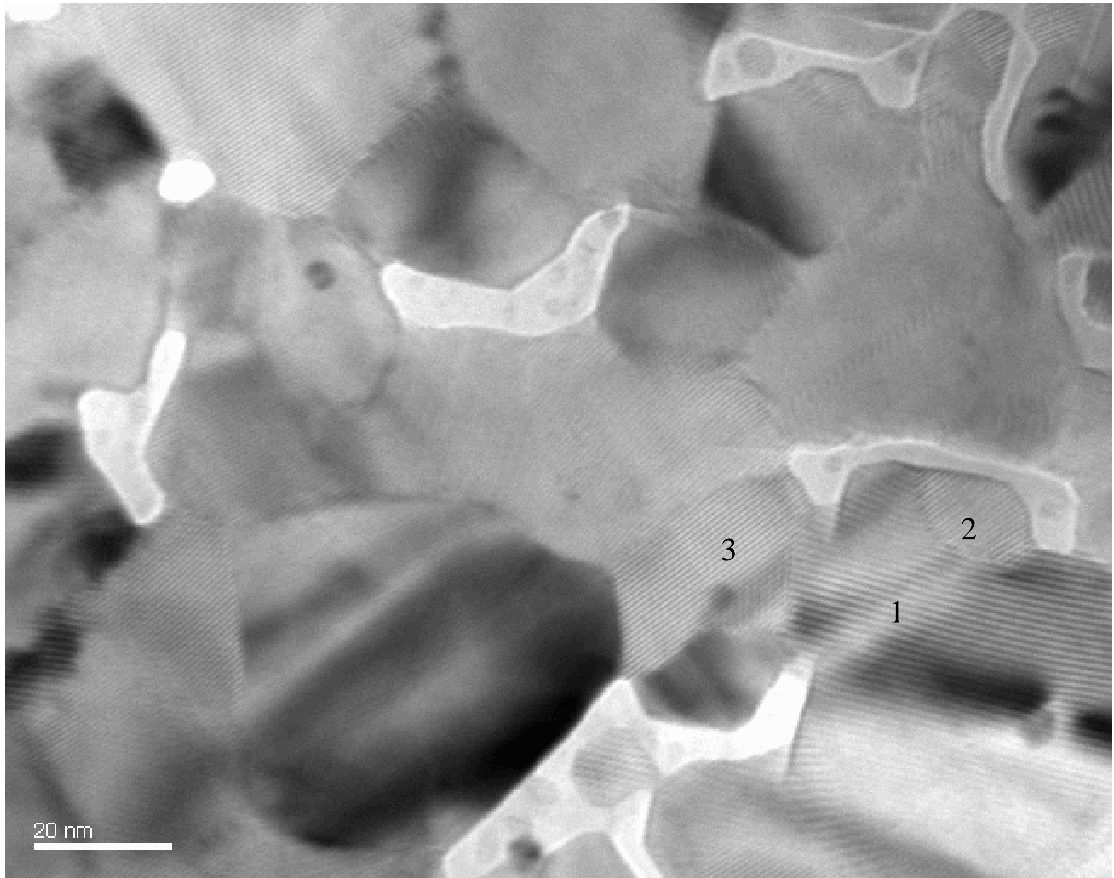

Figure 5.4 The moiré fringe shows the different orientation on one single island, temperature: 100ºC, nominal thickness=37.4nm.

Growth at higher substrate temperatures resulted in the formation of increasingly smaller numbers of larger islands, with more substantial dynamic changes in island profiles being observed upon coalescence due to the increased mobility of Ni species at the higher temperatures.

The islands also exhibited more highly facetted structures, and a representative example is shown in Figure 5.5 (a). In this case, the film was deposited at a substrate temperature of 380ºC, and the images were recorded at a nominal film thickness of 4.3nm. The facets are expected to form on relatively low index (and therefore relatively low surface energy) faces of the deposit material, and this is indeed the case.

Facets along the in-plane [100] and [110] directions can be readily discerned in the figure.

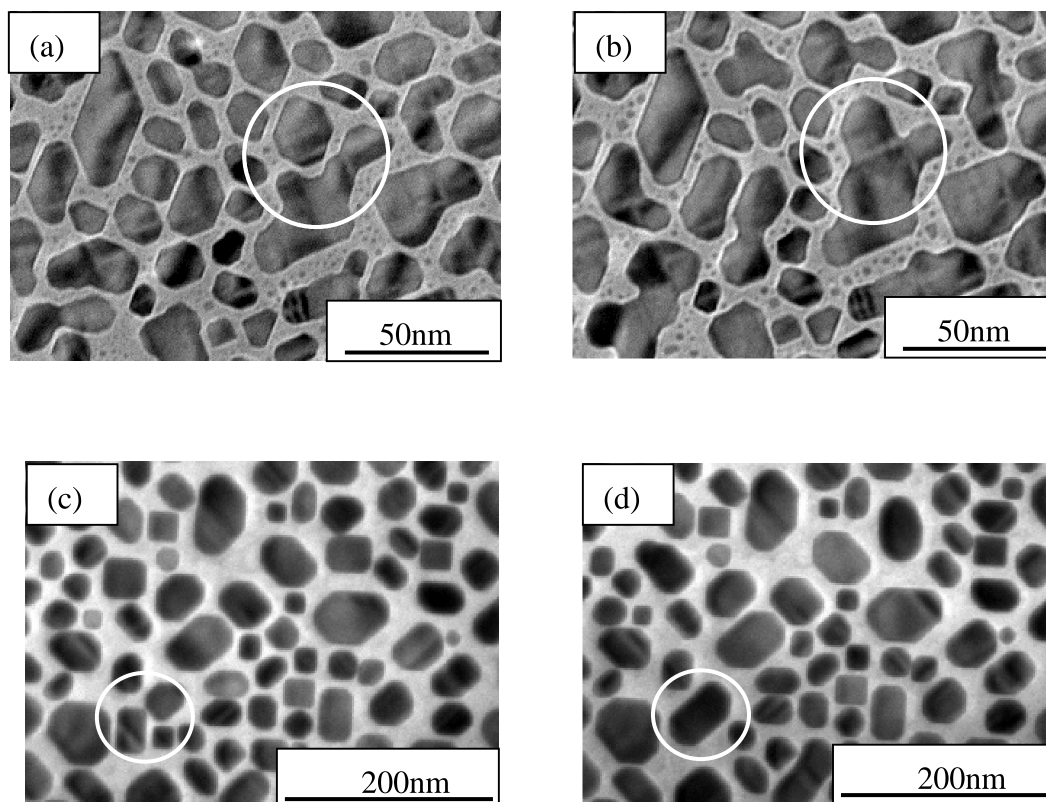

Figure 5.5 Bright field images of Ni films deposited at (a) and (b): 380ºC, (c) and (d): 550ºC, indicating the different coalescence phenomena under different growth temperatures.

Figure 5.5 (b) shows the same area of the sample shown in Figure 5.5 (a), the image being recorded 600s later. The coalescence of several islands took place during the interim period, one example being circled in the figures.

In Figure 5.5 (c) and (d) we present images obtained during deposition at 550ºC, recorded a period of 120s apart at a film thickness of 10nm. Again, a number of coalescence events occurred in the period between the recording of the two images. Real-time video recordings show coalescence to occur almost instantaneously, with substantial dewetting of the substrate being observed. The initiation of the coalescence

of the islands was carefully analysed from real-time video tapes and still images recorded with the slow-scan CCD camera. The nucleation of small, secondary island nuclei between the primary islands on exposed areas of the substrate were observed to be occurring. In some cases, the secondary islands grew to impinge upon a primary island and were subsequently absorbed by the primary island. However, as the primary islands increased in size, and the distance between the edges of primary islands decreased, the secondary nuclei were, in some cases, able to bridge the gap between primary islands, forming a continuous pathway between them. Under the influence of surface tension, the islands then rapidly coalesced to form a single, larger island. In order to minimize island surface area, and contact area between deposit and substrate material, substantial shape changes were observed upon coalescence, maintaining a relatively high aspect ratio to the islands. This process resulted in increased dewetting of the substrate surface at higher growth temperatures.

5.3 Magnetic Properties (MOKE)

To investigate the magnetic properties of the films, *ex-situ* measurements using a longitudinal Magneto-Optic Kerr Effect (MOKE) system were performed. Azimuthal measurements of the magnitude of the magnetic coercivity were made at room temperature as a function of sample orientation by rotation about [001].

As discussed in Chapter 2, Lukaszew et al[5] previously performed STM imaging of both annealed and non-annealed Ni thin films deposited at 100°C by MBE. In the

images acquired from films *in-situ* annealed for ~8 hours at a temperature of ~300°C, a periodic nano-stripe pattern being observed over the surface[5]. The stripes were aligned along in-plane <110> directions, and are believed to correspond to two types of energetically degenerate domains, rotated by 90º with respect to the other. In the case of an equal proportion of these (a 50:50 mixture), the sample would be expected to show a four-fold symmetric magnetic anisotropy. If one stripe domain were to dominate, however (if, for example, during annealing one domain might grow at the expense of the other), the effect would be to superimpose a uniaxial magnetic anisotropy on the magnetocrystalline anisotropy of the un-annealed case.

Before discussing on the MOKE data, it is worth visiting the bright field images and the diffraction patterns which indicate the structure state before and after annealing. Figure 5.6 shows the sample that was grown to a thickness of 20nm at 100ºC, and subsequently annealed at 300ºC for 5 hours.

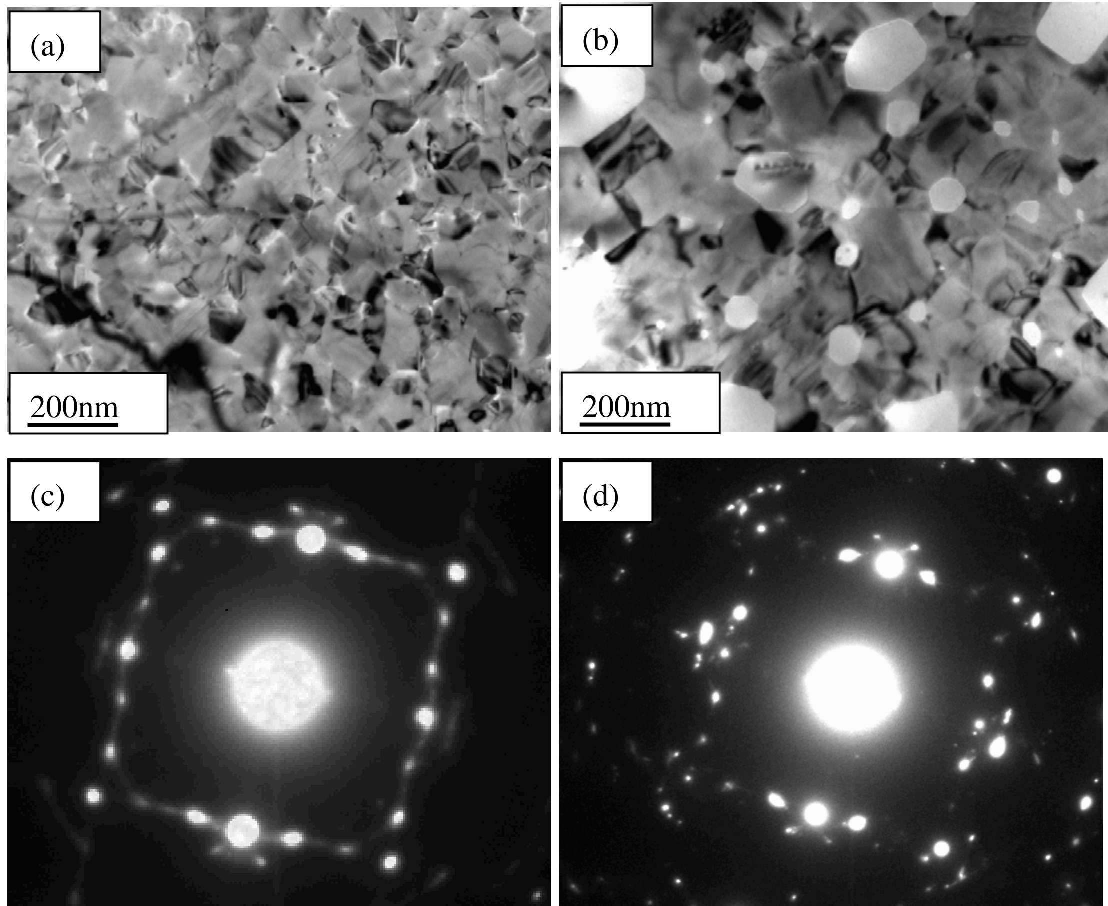

Figure 5.6 Bright field images and sadps of the MOKE sample: a) bf before annealing; b) bf after 5h's annealing; c) sadp before annealing; d) sadp after 5h's annealing.

From Figure 5.6, we can see there are no obvious structural transformations during the high temperature annealing; however, the film has clearly begun to agglomerate, with substantial dewetting of the MgO surface being apparent.

In Figure 5.7 (a) and (b) we present the magnetic data acquired from the MOKE system from films deposited *in-situ* at substrate temperatures of 100°C; in the case of the film of Figure 5.7(a), the film was cooled to room temperature and removed from the system immediately after growth. The data presented in Figure 5.7 (b) was recorded from the sample of Figure 5.6, i.e. it was annealed at a temperature of 300° C *in-situ* for 5 hours prior to being removed from the growth system.

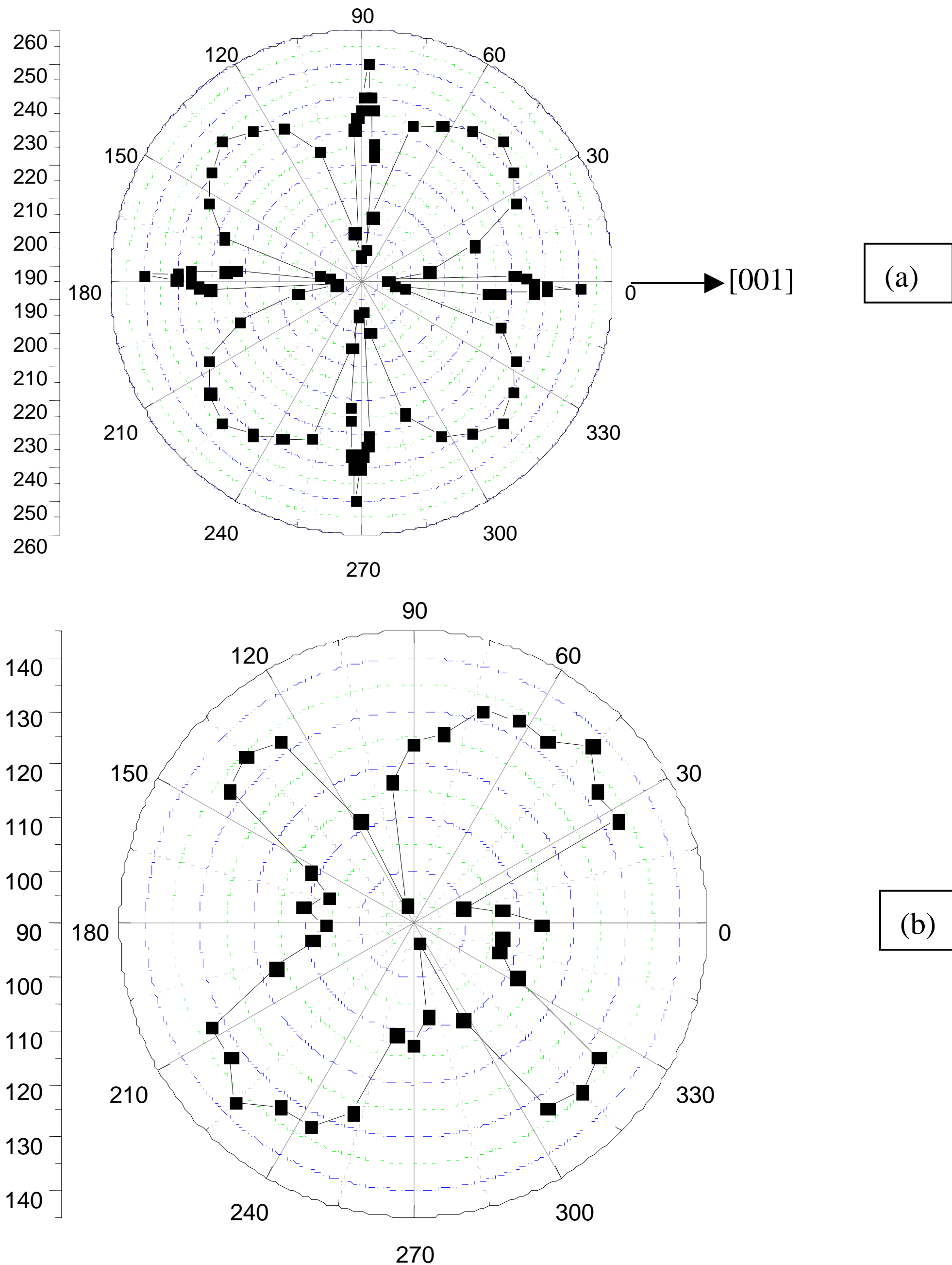

Fig 5.7 MOKE data obtained from Ni thin film of 100ºC growth temperature: (a) immediately after growth; (b) after *in-situ* annealed at a temperature of 300ºC for 5 hours.

Both of the azimuthal MOKE plots presented in Figure 5.7 show the typical four-fold symmetry expected for *fcc* epitaxial films dominated by magnetocrystalline anisotropy. In the case of the annealed film of Figure 5.7 (b), a strong uniaxial

anisotropy is apparently superimposed on the four-fold magnetocrystalline anisotropy of the unannealed film.

Our *in-situ* TEM experiments, all of which are conducted in the plan-view geometry, were not sensitive to the presence of the surface nanopatterning in the case of these samples, since the modulation represents a very small variation in Ni film thickness in proportion to the overall Ni film thickness.

However, our observations do confirm that there is no obvious change in the bulk structure of the films, in addition to any surface stripe formation, which might result in the imposition of a uniaxial magnetic anisotropy.

References:

[1] J. A. Venables, *Introduction to Surface and Thin Film Processes*, (New York : Cambridge University Press, 2000).
[2] L. S. Perkins and A. E. Depristo, Surf. Sci., 325, 169 (1995).
[3] U. Kürpick and T. S. Rahman, Phys. Rev. B, 59, 11014 (1999).
[4] G. Pacchioni and N. Rosch, J. Chem. Phys., 104, 7329 (1996).
[5] R. A. Lukaszew, Z. Zhang, V. Stoica and R. Clarke, Appl. Surf. Sci., 219, 74 (2003).

CHAPTER 6 Conclusion

The growth of Ni thin films deposited on the (001) face of MgO has been studied by ultra-high vacuum *in-situ* transmission electron microscopy and diffraction. The deposition temperatures varied from room temperature to 550ºC.

In all cases the films were found to grow according to a Volmer-Weber growth mode. At the earliest measurable stages of growth, clear evidence of a novel pseudomorphically strained hexagonal close-packed (*hcp*) Ni phase was observed, which subsequently transformed to the expected face centered cubic (*fcc*) phase with further growth. The presence of a small proportion of *fcc* Ni of cube-on-cube (100) orientation was observed to coexist with the *hcp* phase.

The reduction of misfit strain energy is believed to be the driving force for the formation of *hcp* nanosized Ni islands on MgO (001), despite the higher lattice energy of *hcp* relative to *fcc* Ni. Strong Ni-O bonds are formed as the first monolayer of Ni is deposited, with subsequent Ni atoms tending to locate at positions above four nearest-neighbour Ni atoms in the first monolayer. The close-packed structure preferred by Ni can thus be preserved in the plane perpendicular to one of the <100> directions of MgO.

Over the thickness range ~3.6-4.8nm, transformation between the *hcp* and *fcc* structures was observed, and are believed to form by the well known Martensitic transformation. At temperatures below 550°C, both (110) and (100) orientated *fcc* Ni

were present following transformation of the *hcp* phase. At temperatures of 550°C and above, only (100) oriented *fcc* was present. These early stages of the growth of Ni on (100) MgO have not been previously studied and we believe the observations may be understood in terms of a competition between the minimization of interfacial strain energy versus surface energy. Below ~550°C, the reduction in interfacial free energy due to the presence of (110) oriented Ni, of considerably lower lattice mismatch than (100) oriented Ni, is predominant over the increased surface energy of the (110) surface. At 550°C and above, surface energy predominates, and the film assumes the (100) orientation. The (110) oriented film exhibits a twinned microstructure which will also be of increased free energy with respect to the untwinned (100) oriented film.

Studies of our films using the magneto-optic Kerr Effect (MOKE) reveal the presence of a novel uniaxial magnetic anisotropy, following an *in-situ* annealing of our *in-situ* grown films. Our results reveal no significant change in the overall microstructure of the films, which support the previous proposal that the phenomenon may arise due to a novel nano-‘stripe’ pattern, formed during annealing.

Further Work

Future investigation could be carried out on the epitaxial relationship of Ni thin films grown on MgO (111), and a comparison of surface diffusivities on this surface with respect to (100) MgO would be instructive. EELS (Electron Energy Loss Spectroscopy) could be used to investigate the Ni-O bonding at the film-substrate

interface.